

# High-resolution boundary variation diminishing scheme for two-phase compressible flow with cavitation and evaporation

Hiro Wakimura<sup>a,\*</sup>, Tatsuin Li<sup>a</sup>, Keh-Ming Shyue<sup>b</sup>, Takayuki Aoki<sup>c</sup>, Feng Xiao<sup>a,\*</sup>

<sup>a</sup> Department of Mechanical Engineering, Tokyo Institute of Technology, 2-12-1 i6-29 Ookayama, Meguro-ku, Tokyo, 152-8550, Japan

<sup>b</sup> Department of Mathematics and Institute of Applied Mathematical Sciences, National Taiwan University, Taipei 10617, Taiwan

<sup>c</sup> Global Scientific Information and Computing Center, Tokyo Institute of Technology, 2-12-1 i7-3 Ookayama, Meguro-ku, Tokyo 152-8550, Japan

## ARTICLE INFO

### Keywords:

Compressible multiphase flow  
Phase change  
Finite volume method  
Boundary variation diminishing  
Low dissipation

## ABSTRACT

We propose high-resolution numerical schemes for two-phase compressible flow simulations to reproduce dynamically created gas/vapor-liquid interfaces with phase change. In the Godunov-type finite volume framework, suppressing numerical dissipation errors in numerical schemes is crucial for capturing the discontinuous solutions. The MUSCL scheme has second-order accuracy for smooth solutions and non-oscillatory behavior near discontinuous solutions. However, the MUSCL scheme introduces excessive numerical dissipation and diffuses the discontinuities nonphysically, leading to difficulties in distinguishing gas/vapor and liquid phases, and thus causing a blur in the interfaces during the multi-phase flow simulations.

The hybrid-type boundary variation diminishing (BVD) scheme in this paper combines the MUSCL scheme and the THINC scheme to reduce the numerical dissipation errors near the discontinuities. The MUSCL-THINC-BVD scheme applies the MUSCL scheme for smooth solutions and the THINC scheme for discontinuous solutions, resulting in the successful capture of the discontinuities including the dynamically created gas/vapor-liquid interfaces. The Adaptive THINC-BVD scheme, which switches two types of THINC schemes with different values of gradient parameter, also captures the discontinuities clearly. The numerical results of the benchmark tests show that the proposed BVD schemes can lucidly reproduce the vapor-liquid interfaces newly created during the dynamical process of phase change.

## 1. Introduction

The compressible gas/vapor-liquid two-phase flows with cavitation and evaporation are observed in various engineering situations, such as propellers, airfoils, hydraulic systems, and so on. The flow field simultaneously has smooth solutions and discontinuous solutions, like vortices, rarefaction waves, shock waves, contact discontinuities, and gas/vapor-liquid interfaces. Furthermore, discontinuities, such as interfaces, can dynamically form and diminish as phase changes take place. As these flow structures interfere with each other, which makes the flow dynamics extremely complicated, the numerical simulation of such flow remains a challenging issue.

The important issue in the computation of the gas/vapor-liquid two-phase flows is how to numerically deal with the gas/vapor-liquid interfaces. The sharp-interface model (SIM) regards the interface as a sharp discontinuity. Each side of the interface is assumed

\* Corresponding authors.

E-mail addresses: [wakimura.h.aa@m.titech.ac.jp](mailto:wakimura.h.aa@m.titech.ac.jp) (H. Wakimura), [xiao.f.aa@m.titech.ac.jp](mailto:xiao.f.aa@m.titech.ac.jp) (F. Xiao).

<https://doi.org/10.1016/j.jcp.2024.113164>

Received 24 February 2024; Received in revised form 28 May 2024; Accepted 1 June 2024

Available online 7 June 2024

0021-9991/© 2024 Elsevier Inc. All rights are reserved, including those for text and data mining, AI training, and similar technologies.

to be filled with a bulk fluid of gas or liquid. The Volume-of-Fluid (VOF) method [1–3], level-set method [4,5], and front-tracking method [6,7] are typical methods to compute the location of interface. Although the SIM is widely used to track the interface in the incompressible multiphase flow simulations, it is reported [8] that these methods are not able to solve interfaces separating pure fluid and mixtures and to dynamically create the interface as seen in phase change phenomenon. On the other hand, the diffuse-interface model (DIM) deals with the interface as a numerical mixture region. The gas and liquid are artificially relaxed and mixed in this region, where a state of numerically consistent thermodynamic laws is reached [8]. The main advantages of DIM are the simplicity of using the same computational algorithm over the entire computational domain, the ease of ensuring conservation of mixed mass, momentum, and energy, and the ability to naturally reproduce dynamically created interfaces. Conversely, the disadvantage of DIM is that it requires a method to prevent non-physical diffusion of the interface due to numerical dissipation errors.

Various two-fluid numerical models have been developed based on the DIM approach. The seven-equation models [9–11] have conservation laws of mass, momentum, and energy for each phase and the VOF transport equation. In [10], the pressure and velocity are assumed to reach equilibrium states at infinite rates. After that, the five-equation models [12–15] were developed reducing the number of equations and eliminating the relaxation source terms in the seven-equation model. Because of its simplicity, the five-equation models have been widely used as the governing equations for the compressible two-phase flow. However, since the mixture sound speed of Kapila's five-equation model, which is called the "sound speed of Wood", has non-monotonic behavior to the volume fraction, it has been reported that the transport of the mixture zone is possible to be numerically unstable [8,16]. The six-equation models [8,11,17,18] solved this problem by applying pressure relaxation term into one-velocity two-pressure form. Heat and mass transfer were implemented [11,17] by adding thermal and chemical relaxation terms into the six-equation model. In [18], the six-equation model was proposed so as to be consistent with the conservation of total mixture energy, and allows for a more simple and efficient numerical method for chemical relaxation. In this work, we use the six-equation model [18] as the governing equations of the two-phase compressible flow.

Another long-standing drawback of the Eulerian numerical frameworks is the numerical dissipation which makes the discontinuities vanish as the computational time lasts. The dissipation is particularly crucial in the multi-phase fluid simulation, as the numerical dissipation blurs the interfaces separating different phases and makes them difficult to identify. Godunov finite-volume method [19], which was proposed originally for the single phase flow, now becomes the primary methodology to solve the DIM model in the multi-phase flows.

Many high-order accuracy schemes have been so far developed under the framework of the Godunov-type finite-volume method. The MUSCL (Monotone Upstream-centered Schemes for Conservation Law) [20] and WENO (Weighted Essentially Non-Oscillatory) [21–23] schemes have been widely recognized as the mainstream high-order numerical schemes. Also, the MP5 (Fifth-order Monotonicity Preserving) [24] and MP5-R (fifth-order improved MP scheme) [25] schemes are well recognized. The MUSCL scheme employs piecewise-linear interpolation and introduces the slope limiter that restricts the gradient of the interpolation function to achieve second-order accuracy and satisfy TVD (Total Variation Diminishing) [26] property. Because of its computational stability, the MUSCL scheme is widely used in various applications. The WENO scheme achieves high-order accuracy and essentially avoids the numerical oscillation error near the discontinuities by weighting the multiple interpolations in sub-stencils according to the smoothness of the numerical solution. However, both the MUSCL and WENO schemes are known to include numerical dissipation errors introduced by nonlinear limiters that increase with time evolution. This numerical dissipation error is significant specifically in high-frequency waves. Thus, the discontinuous solutions (e.g., shock wave, contact discontinuity, and gas/vapor-liquid free interface) and small-scale vortex in turbulence flow diffuse nonphysically due to the excessive numerical dissipation error. The significantly diffused flow structures make it difficult to implement and reproduce interfacial phenomena like phase change. The stable and low-dissipation computation of high-frequency solutions in compressible flows remains a crucial challenge in the Godunov-type numerical schemes.

Focusing on numerical simulations of the compressible gas/vapor-liquid two-phase flows with phase transition, in our knowledge, there have been few studies that report dynamically created interfaces clearly captured in multidimensional tests. Generally, in the DIM models the initial size of the dynamically created bubble or droplet by phase change is smaller compared to a computational mesh, and thus the new interface is sensitive to the artificial viscosity in the numerical scheme. To keep the dynamically generated interface from vanishing, a numerical scheme that does not diffuse discontinuities is essential.

Stemming from using merely the continuous reconstruction functions in each stencil meshes, the numerical dissipation has posed the persistent and unresolved challenge for the Eulerian formulations. A class of Godunov-type numerical methods has been reported that low-dissipation numerical schemes can be constructed based on the BVD (Boundary Variation Diminishing) principle [27–37]. The BVD principle suggests that the difference between left- and right-side values interpolated on the cell boundary should be minimized to reduce the numerical dissipation error. The BVD strategy is often incorporated into the hybrid-type numerical scheme as the algorithm to select an appropriate scheme at each computational cell. For example, the MUSCL-THINC-BVD scheme [28] has two candidate interpolants: the MUSCL scheme and the THINC (Tangent Hyperbola for INterface Capturing) scheme [38,39], and chooses an appropriate one using the BVD selection algorithm. The MUSCL scheme has second-order accuracy for the smooth solution, and the THINC scheme captures the discontinuous solution without introducing the unnecessary numerical dissipation error. Since the BVD algorithm selects the MUSCL scheme in the smooth solution and the THINC scheme in the discontinuous solution which allows a discontinuous reconstruction in corresponding cell, the MUSCL-THINC-BVD scheme achieves low numerical dissipation errors in both the smooth and discontinuous solutions. This property is crucial for the DIM for the multiphase flow simulation to suppress the excessive numerical dissipation error in the gas-liquid interface. Some BVD schemes have already demonstrated that the discontinuities in the compressible multiphase flows are captured clearly despite the complex deformation of interfaces [28,34,40].

In this work, we apply the BVD schemes to the compressible two-phase flow with phase change and demonstrate that the BVD schemes reduce the numerical dissipation errors and keep the dynamically created interfaces well identified from vanishing.

Considering that a numerical scheme that has accuracy higher than third-order may introduce spurious oscillation error due to the reconstruction of primitive variables, we use second-order BVD schemes like MUSCL-THINC-BVD [28] and Adaptive THINC-BVD [29] schemes. We employ numerical tests which are typical for compressible two-phase flows where the interfaces are dynamically generated by phase change to showcase the capability of the BVD. The numerical results indicate that the BVD schemes preserve clearly the interfaces created by the phase change, whereas the traditional scheme fails to identify the interfaces due to the too-large numerical dissipation.

The rest of this paper is organized as follows. In section 2, the six-equation model [18] without and with phase change is briefly introduced. In section 3, the low-dissipation numerical schemes based on the BVD principle are described. The numerical results of benchmark tests are shown in section 4. The conclusion is given in section 5 to end this paper.

## 2. Governing equations

### 2.1. Six-equation two-phase model

To solve the compressible two-phase flow, we adopt the six-equation model proposed by Pelanti and Shyue [18],

$$\frac{\partial \alpha_1}{\partial t} + \mathbf{u} \cdot \nabla \alpha_1 = \mu(p_1 - p_2), \quad (1a)$$

$$\frac{\partial(\alpha_1 \rho_1)}{\partial t} + \nabla \cdot (\alpha_1 \rho_1 \mathbf{u}) = 0, \quad (1b)$$

$$\frac{\partial(\alpha_2 \rho_2)}{\partial t} + \nabla \cdot (\alpha_2 \rho_2 \mathbf{u}) = 0, \quad (1c)$$

$$\frac{\partial(\rho \mathbf{u})}{\partial t} + \nabla \cdot (\rho \mathbf{u} \otimes \mathbf{u} + (\alpha_1 p_1 + \alpha_2 p_2) \mathbb{I}) = \mathbf{0}, \quad (1d)$$

$$\frac{\partial(\alpha_1 E_1)}{\partial t} + \nabla \cdot (\alpha_1 (E_1 + p_1) \mathbf{u}) + \Sigma = -\mu p_1 (p_1 - p_2), \quad (1e)$$

$$\frac{\partial(\alpha_2 E_2)}{\partial t} + \nabla \cdot (\alpha_2 (E_2 + p_2) \mathbf{u}) - \Sigma = \mu p_1 (p_1 - p_2), \quad (1f)$$

where  $\alpha_k$  is volume fraction,  $\rho_k$  is phasic density,  $\mathbf{u} = (u, v, w)^\top$  is velocity vector,  $E_k$  is phasic total energy, and  $p_k$  is phasic pressure. Variables with the subscript  $k$  ( $k = 1, 2$ ) indicate that they are physical quantities of the  $k$ -th phase, while variables without subscript represent mixture quantities of the two phases. The mixture quantities are defined to be consistent in the artificial mixture region in the DIM. The mixture rules of the volume fraction, density, internal energy, and total energy are respectively given as,

$$\alpha_1 + \alpha_2 = 1, \quad (2a)$$

$$\alpha_1 \rho_1 + \alpha_2 \rho_2 = \rho, \quad (2b)$$

$$\alpha_1 \mathcal{E}_1 + \alpha_2 \mathcal{E}_2 = \mathcal{E}, \quad (2c)$$

$$\alpha_1 E_1 + \alpha_2 E_2 = E, \quad (2d)$$

where  $\mathcal{E}_k = E_k - \frac{1}{2} \rho_k \|\mathbf{u}\|^2$  is phasic internal energy.

The non-conservative term  $\Sigma$  appearing in the phasic total energy equations (1e) and (1f) reads,

$$\Sigma = -\mathbf{u} \cdot (Y_2 \nabla(\alpha_1 p_1) - Y_1 \nabla(\alpha_2 p_2)), \quad (3)$$

where  $Y_k = \frac{\alpha_k \rho_k}{\rho}$  is a mass fraction of phase  $k$  ( $Y_1 + Y_2 = 1$ ). Note that  $\alpha_1$ ,  $\alpha_1 E_1$ , and  $\alpha_2 E_2$  are not indeed conservative.

The source terms appearing in (1a), (1e), and (1f) act to ensure that the mechanical equilibrium across the interface is satisfied, where  $\mu > 0$  is pressure relaxation parameter and  $p_1$  is interface pressure. An infinite-rate pressure relaxation is assumed with  $\mu \rightarrow \infty$ , hence mechanical equilibrium is reached instantaneously.

### 2.2. Stiffened gas equation of state (SG EOS)

To close the system (1), we introduce the equation of states for each phase. For solving the system without heat and mass transfer, we need to specify only the pressure law  $p_k = p_k(\mathcal{E}_k, \rho_k)$ . However, with heat and mass transfer, we need in addition the caloric law  $T_k = T_k(p_k, \rho_k)$ , where  $T_k$  is the phasic temperature, to completely describe the thermodynamic state of the fluid [18]. With the SG EOS assumption, the pressure  $p_k$  and the temperature  $T_k$  are given as,

$$p_k(\mathcal{E}_k, \rho_k) = (\gamma_k - 1)(\mathcal{E}_k - \eta_k \rho_k) - \gamma_k \pi_k, \quad (4a)$$

$$T_k(p_k, \rho_k) = \frac{p_k + \pi_k}{(\gamma_k - 1)C_{v,k} \rho_k}, \quad (4b)$$

and associated phasic specific entropy  $s_k$  and phasic specific Gibbs energy  $g_k$  are given as,

$$s_k(p_k, T_k) = C_{vk} \ln \frac{T_k^{\gamma_k}}{(p_k + \pi_k)^{\gamma_k - 1}} + \eta'_k, \quad (4c)$$

$$g_k(p_k, T_k) = h_k - T_k s_k \\ = (\gamma_k C_{vk} - \eta'_k) T_k - C_{vk} T_k \ln \frac{T_k^{\gamma_k}}{(p_k + \pi_k)^{\gamma_k - 1}} + \eta_k, \quad (4d)$$

where  $\gamma_k, \pi_k, C_{vk}, \eta_k, \eta'_k$  are material-dependent parameters,  $h_k = \frac{\mathcal{E}_k + p_k}{\rho_k}$  is phasic specific enthalpy.

With isobaric assumption  $p_1 = p_2 = p$  in the mixture rule of the internal energy (2c):

$$\alpha_1 \mathcal{E}_1(p, \rho_1) + \alpha_2 \mathcal{E}_2(p, \rho_2) = \mathcal{E}, \quad (5)$$

we can obtain an explicit expression of mixture pressure  $p$  as,

$$p = \frac{\mathcal{E} - (\alpha_1 \rho_1 \eta_1 + \alpha_2 \rho_2 \eta_2) - \left( \frac{\alpha_1 \gamma_1 \pi_1}{\gamma_1 - 1} + \frac{\alpha_2 \gamma_2 \pi_2}{\gamma_2 - 1} \right)}{\frac{\alpha_1}{\gamma_1 - 1} + \frac{\alpha_2}{\gamma_2 - 1}}. \quad (6)$$

### 2.3. Mixture sound speed

According to the pressure formula of the SG EOS (4a), the phasic sound speed  $c_k$  can be derived as,

$$c_k = \sqrt{\frac{\partial p(\mathcal{E}_k, \rho_k)}{\partial \rho_k} + h_k \frac{\partial p(\mathcal{E}_k, \rho_k)}{\partial \mathcal{E}_k}} \\ = \sqrt{\frac{\gamma_k (p_k + \pi_k)}{\rho_k}}. \quad (7)$$

Then, the mixture sound speed of the model (1) (without heat and mass transfer) is expressed as,

$$c = \sqrt{Y_1 c_1^2 + Y_2 c_2^2}. \quad (8)$$

This type of the mixture sound speed is called ‘‘frozen sound speed’’ [41,42], and is known to have monotonicity with respect to the volume fraction [18]. This monotonicity property helps avoid numerical oscillation errors in the mixture region [8].

### 2.4. Heat and mass transfer model

The heat and mass transfer effects have been treated by introducing additional thermal and chemical relaxation terms (cf. [10, 11, 18, 43–46]). Following this way, the six-equation model with heat and mass transfer takes the form:

$$\frac{\partial \alpha_1}{\partial t} + \mathbf{u} \cdot \nabla \alpha_1 = \mu(p_1 - p_2) + \frac{Q}{\kappa} + \frac{\dot{m}}{\rho_1}, \quad (9a)$$

$$\frac{\partial(\alpha_1 \rho_1)}{\partial t} + \nabla \cdot (\alpha_1 \rho_1 \mathbf{u}) = \dot{m}, \quad (9b)$$

$$\frac{\partial(\alpha_2 \rho_2)}{\partial t} + \nabla \cdot (\alpha_2 \rho_2 \mathbf{u}) = -\dot{m}, \quad (9c)$$

$$\frac{\partial(\rho \mathbf{u})}{\partial t} + \nabla \cdot (\rho \mathbf{u} \otimes \mathbf{u} + (\alpha_1 p_1 + \alpha_2 p_2) \mathbb{I}) = \mathbf{0}, \quad (9d)$$

$$\frac{\partial(\alpha_1 E_1)}{\partial t} + \nabla \cdot (\alpha_1 (E_1 + p_1) \mathbf{u}) + \Sigma = -\mu p_1 (p_1 - p_2) + Q + e_1 \dot{m}, \quad (9e)$$

$$\frac{\partial(\alpha_2 E_2)}{\partial t} + \nabla \cdot (\alpha_2 (E_2 + p_2) \mathbf{u}) - \Sigma = \mu p_1 (p_1 - p_2) - Q - e_1 \dot{m}, \quad (9f)$$

where  $Q = \theta(T_2 - T_1)$ ,  $\dot{m} = v(g_2 - g_1)$  are thermal relaxation term and chemical relaxation term, respectively. Although the parameters  $\kappa, \rho_1$  (interface density),  $e_1$  (interface specific total energy) can be derived by imposing appropriate thermodynamic constraint [11], we assume infinite-rate relaxations for thermal and chemical equilibrium, and the specific formulas of  $\kappa, \rho_1$ , and  $e_1$  are not required in the relaxation calculations [18]. We activated the thermal and chemical relaxations only at the liquid-gas interface to reduce computational costs. Since these relaxations have minimal impact far from the interfaces, we found that this approach does not affect the numerical solution, provided that the problem-dependent parameter  $e_1$  in equations (10) and (11) is sufficiently small. Moreover, we consider evaporation but not condensation, so the chemical relaxation is activated under a metastable state (the liquid temperature  $T_{\text{liq}}$  is higher than the saturation temperature  $T_{\text{sat}}(p)$  at the given pressure). Hence, the relaxation parameters  $\theta$  and  $v$  are determined as,

**Table 1**  
SGEOS parameters of water for 300-500 K.

		$\gamma$	$\pi$ [Pa]	$\eta$ [J/kg]	$\eta'$ [J/(kg K)]	$C_v$ [J/(kg K)]
water	liquid	2.35	$10^9$	$-1167 \times 10^3$	0	1816
	vapor	1.43	0	$2030 \times 10^3$	$-23.4 \times 10^3$	1040

**Table 2**  
SGEOS parameters of dodecane for 300-500 K.

		$\gamma$	$\pi$ [Pa]	$\eta$ [J/kg]	$\eta'$ [J/(kg K)]	$C_v$ [J/(kg K)]
dodecane	liquid	2.35	$4 \times 10^8$	$-775.269 \times 10^3$	0	1077.7
	vapor	1.025	0	$-237.547 \times 10^3$	$-24.4 \times 10^3$	1956.45

$$\theta = \begin{cases} \infty & \text{if } \epsilon_1 \leq \alpha_1 \leq 1 - \epsilon_1, \\ 0 & \text{otherwise,} \end{cases} \quad (10)$$

$$v = \begin{cases} \infty & \text{if } \epsilon_1 \leq \alpha_1 \leq 1 - \epsilon_1 \text{ and } T_{\text{liq}} > T_{\text{sat}}(p), \\ 0 & \text{otherwise,} \end{cases} \quad (11)$$

where parameter  $\epsilon_1 = 10^{-4}$  indicates the interface location. The influence of this parameter  $\epsilon_1$  is under small perturbation, provided that  $\epsilon_1$  is sufficiently small.

The pressure-temperature (p-T) saturation curve under the SG EOS assumption can be obtained from the chemical equilibrium condition,  $g_1 = g_2$  [43,47]. Using the formula of Gibbs energy (4d) of each phase, the p-T saturation curve is determined as an implicit function of pressure and temperature as follows,

$$A_s + \frac{B_s}{T} + C_s \ln T + D_s \ln(p + \pi_1) - \ln(p + \pi_2) = 0, \quad (12)$$

with

$$A_s = \frac{C_{p1} - C_{p2} + \eta'_2 - \eta'_1}{C_{p2} - C_{v2}}, \quad B_s = \frac{\eta_1 - \eta_2}{C_{p2} - C_{v2}}, \quad C_s = \frac{C_{p2} - C_{p1}}{C_{p2} - C_{v2}}, \quad D_s = \frac{C_{p1} - C_{v1}}{C_{p2} - C_{v2}}. \quad (13)$$

Here,  $C_{pk} = \gamma_k C_{vk}$  is a heat capacity of phase  $k$  with constant pressure. The material-dependent parameters in the SG EOS (4) can be set so that the p-T saturation curve (12) fits the experimental curve [47]. We use the values of the SGEOS parameters as in Table 1 for water and Table 2 for dodecane that have been adopted in [18,43].

In later explanations, to simply refer to the equations (1) and (9), we denote  $\mathbf{q} = (\alpha_1, \alpha_1 \rho_1, \alpha_2 \rho_2, \rho \mathbf{u}, \alpha_1 E_1, \alpha_2 E_2)^T$  as a vector of solution variables and express the equations in a compact form:

$$\frac{\partial \mathbf{q}}{\partial t} + \nabla \cdot \mathbf{f}(\mathbf{q}) + \sigma(\mathbf{q}, \nabla \mathbf{q}) = \psi_p(\mathbf{q}) \quad (\text{without heat and mass transfer}), \quad (14)$$

and

$$\frac{\partial \mathbf{q}}{\partial t} + \nabla \cdot \mathbf{f}(\mathbf{q}) + \sigma(\mathbf{q}, \nabla \mathbf{q}) = \psi_p(\mathbf{q}) + \psi_T(\mathbf{q}) + \psi_g(\mathbf{q}) \quad (\text{with heat and mass transfer}), \quad (15)$$

where

$$\mathbf{q} = \begin{bmatrix} \alpha_1 \\ \alpha_1 \rho_1 \\ \alpha_2 \rho_2 \\ \rho \mathbf{u} \\ \alpha_1 E_1 \\ \alpha_2 E_2 \end{bmatrix}, \quad \mathbf{f}(\mathbf{q}) = \begin{bmatrix} \mathbf{0} \\ \alpha_1 \rho_1 \mathbf{u} \\ \alpha_2 \rho_2 \mathbf{u} \\ \rho \mathbf{u} \otimes \mathbf{u} + (\alpha_1 p_1 + \alpha_2 p_2) \mathbb{I} \\ \alpha_1 (E_1 + p_1) \mathbf{u} \\ \alpha_2 (E_2 + p_2) \mathbf{u} \end{bmatrix}, \quad \sigma(\mathbf{q}, \nabla \mathbf{q}) = \begin{bmatrix} \mathbf{u} \cdot \nabla \alpha_1 \\ 0 \\ 0 \\ \mathbf{0} \\ \Sigma \\ -\Sigma \end{bmatrix}, \quad (16)$$

$$\psi_p(\mathbf{q}) = \begin{bmatrix} \mu(p_1 - p_2) \\ 0 \\ 0 \\ \mathbf{0} \\ -\mu p_1(p_1 - p_2) \\ \mu p_1(p_1 - p_2) \end{bmatrix}, \quad \psi_T(\mathbf{q}) = \begin{bmatrix} \frac{\theta(T_2 - T_1)}{\kappa} \\ 0 \\ 0 \\ \mathbf{0} \\ \theta(T_2 - T_1) \\ -\theta(T_2 - T_1) \end{bmatrix}, \quad \psi_g(\mathbf{q}) = \begin{bmatrix} \frac{v(g_2 - g_1)}{\rho_1} \\ v(g_2 - g_1) \\ -v(g_2 - g_1) \\ \mathbf{0} \\ v e_1(g_2 - g_1) \\ -v e_1(g_2 - g_1) \end{bmatrix}.$$

### 3. Numerical methods

For simply describing the numerical methods, the computational domain is assumed to be 1D and divided into uniform non-overlapping cells  $\Omega_i = \left[ x_{i-\frac{1}{2}}, x_{i+\frac{1}{2}} \right]$ , ( $i = 1, \dots, N$ ), with cell size  $\Delta x = x_{i+\frac{1}{2}} - x_{i-\frac{1}{2}}$ . We note that the numerical methods described below can be applied to multi-dimensional problems straightforwardly in a dimension-by-dimension manner.

We apply the fractional-step method [18] to solve the system (14) and (15). Firstly, the homogeneous hyperbolic portion of the 1D system:

$$\frac{\partial \mathbf{q}}{\partial t} + \frac{\partial \mathbf{f}(\mathbf{q})}{\partial x} + \sigma \left( \mathbf{q}, \frac{\partial \mathbf{q}}{\partial x} \right) = \mathbf{0}, \quad (17)$$

is solved over time interval  $\Delta t$ . After that, based on the solution obtained from solving (17), the ordinary differential equation (ODE) that consists of the remaining part of (14) and (15) (the relaxation terms) is solved. For example, in the case of (14) (without heat and mass transfer), the ODE system becomes,

$$\frac{\partial \mathbf{q}}{\partial t} = \boldsymbol{\psi}_p(\mathbf{q}). \quad (18)$$

When the operation of solving the homogeneous hyperbolic portion of the system (17) and the operation of solving pressure relaxation equation (18) are denoted as  $\mathcal{L}_{\text{hyp}}^{\Delta t}$  and  $\mathcal{L}_p$  respectively (as in [48]), the complete solution of the six-equation model without heat and mass transfer is expressed as,

$$\mathbf{q}^{n+1} = \mathcal{L}_p \mathcal{L}_{\text{hyp}}^{\Delta t} \mathbf{q}^n. \quad (19)$$

In the case of phase change, the additional ODE systems are solved. When the operation of solving thermal and chemical relaxation equations is denoted as  $\mathcal{L}_{pT}$  and  $\mathcal{L}_{pTg}$  respectively, one possible complete solution of the six-equation model with phase change reads,

$$\mathbf{q}^{n+1} = \mathcal{L}_{pTg} \mathcal{L}_{pT} \mathcal{L}_p \mathcal{L}_{\text{hyp}}^{\Delta t} \mathbf{q}^n. \quad (20)$$

The operations  $\mathcal{L}_p$ ,  $\mathcal{L}_{pT}$ , and  $\mathcal{L}_{pTg}$  are corresponding to solving the source terms  $\boldsymbol{\psi}_p(\mathbf{q})$ ,  $\boldsymbol{\psi}_p(\mathbf{q}) + \boldsymbol{\psi}_T(\mathbf{q})$ , and  $\boldsymbol{\psi}_p(\mathbf{q}) + \boldsymbol{\psi}_T(\mathbf{q}) + \boldsymbol{\psi}_g(\mathbf{q})$  respectively in (14) and (15).

In the remainder of this section, the operation of solving the homogeneous hyperbolic portion and relaxation procedures is explained separately. In a framework of the Godunov-type finite-volume method, we describe the high-fidelity reconstruction methods based on BVD principle in section 3.2. The spatial discretization is conducted by the wave-propagation method, described in section 3.3. The calculation procedures of mechanical, thermal, and chemical relaxation are shown in section 3.4. At the end of this section, the overall calculation procedure is summarized in section 3.5.

#### 3.1. Godunov-type finite-volume method

For solving the homogeneous hyperbolic equation (17), we briefly review the calculation procedure of the Godunov-type finite-volume method [19]. The semi-discrete form of the hyperbolic system (17) reads,

$$\frac{d\bar{q}_i(t)}{dt} = -\frac{1}{\Delta x} \left( \mathbf{f} \left( \mathbf{q} \left( x_{i+\frac{1}{2}}, t \right) \right) - \mathbf{f} \left( \mathbf{q} \left( x_{i-\frac{1}{2}}, t \right) \right) \right), \quad (21)$$

where the numerical solution  $\bar{q}_i(t)$  is defined as a volume-integrated average of the computational cell  $\Omega_i$ ,

$$\bar{q}_i(t) \equiv \frac{1}{\Delta x} \int_{x_{i-\frac{1}{2}}}^{x_{i+\frac{1}{2}}} \mathbf{q}(x, t) dx. \quad (22)$$

Here, we omitted the non-conservative term  $\sigma$  in (17) for brevity. In the Godunov-type finite-volume method, the fluxes at cell boundaries  $x = x_{i+\frac{1}{2}}$  and  $x = x_{i-\frac{1}{2}}$  in the right-hand-side of the semi-discrete formula (21) are evaluated as numerical fluxes  $\hat{\mathbf{f}}$ ,

$$\frac{d\bar{q}_i}{dt} \approx -\frac{1}{\Delta x} \left( \hat{\mathbf{f}}_{i+\frac{1}{2}} - \hat{\mathbf{f}}_{i-\frac{1}{2}} \right). \quad (23)$$

The numerical flux  $\hat{\mathbf{f}}_{i+\frac{1}{2}}$  at the cell boundary  $x = x_{i+\frac{1}{2}}$  is calculated by solving the Riemann problem consisting of left- and right-side states of the cell boundary,

$$\hat{\mathbf{f}}_{i+\frac{1}{2}} = \hat{\mathbf{f}}^{\text{Riemann}} \left( \mathbf{q}_{L,i+\frac{1}{2}}, \mathbf{q}_{R,i+\frac{1}{2}} \right), \quad (24)$$

where  $\mathbf{q}_{L,i+\frac{1}{2}}$  and  $\mathbf{q}_{R,i+\frac{1}{2}}$  are interpolated values on the left and right sides of the cell boundary, respectively. The numerical flux  $\hat{\mathbf{f}}_{i+\frac{1}{2}}$  is obtained using an approximate Riemann solver, which is clearly distinguished from the physical flux  $\mathbf{f}(\mathbf{q}(x_{i+\frac{1}{2}}))$ , as the

numerical flux is determined from upstream-biased information resulting in the artificial viscosity. Once the values of the numerical fluxes  $\hat{f}_{i+\frac{1}{2}}$  and  $\hat{f}_{i-\frac{1}{2}}$  are obtained, the time derivative of the numerical solution can be calculated from (23), and the numerical solution can be updated using the ODE solver like Runge-Kutta method [49].

The remaining task is to obtain the left- and right-side cell-boundary values  $q_{L,i+\frac{1}{2}}$  and  $q_{R,i+\frac{1}{2}}$ , which is the most important point for the numerical accuracy in the Godunov-type FVM. The cell-boundary values  $q_{L,i+\frac{1}{2}}$  and  $q_{R,i-\frac{1}{2}}$  are interpolated by the cell-wise reconstruction function  $Q_i(x)$  constructed using information from surrounding numerical solutions  $(\dots, \bar{q}_{i-1}, \bar{q}_i, \bar{q}_{i+1}, \dots)$ , i.e.,  $q_{L,i+\frac{1}{2}} = Q_i(x_{i+\frac{1}{2}})$  and  $q_{R,i-\frac{1}{2}} = Q_i(x_{i-\frac{1}{2}})$ .

Many studies for constructing accurate and robust reconstruction functions have been reported. The MUSCL scheme [20] and the WENO scheme [21–23] are representative reconstruction methods that have high-order accuracy and non-oscillatory property. These schemes have been widely used and researched over two decades, however, as we mentioned before, they have problems of too large numerical dissipation error especially for high-frequency solutions. This excessive numerical dissipation error is known to non-physically smear the short wavelength flow structures such as shock waves, contact discontinuity, small-scale vortices, and so on. Especially, in our knowledge, the dynamically created gas/vapor-liquid interfaces in the two-phase flows with phase change have never been captured due to the significant numerical dissipation error. To solve this problem, we need high-fidelity schemes that capture both smooth and discontinuous solutions simultaneously.

### 3.2. High-fidelity reconstruction method

We propose high-fidelity reconstruction methods that reduce the numerical dissipation error in the discontinuous solutions based on the boundary variation diminishing (BVD) principle. In this section, we firstly explain about the BVD principle, and next each candidate reconstruction function, BVD selection algorithm.

#### 3.2.1. Boundary variation diminishing (BVD) principle

We consider the 1D scalar advection equation:

$$\frac{\partial q(x, t)}{\partial t} + \frac{\partial f(q(x, t))}{\partial x} = 0, \tag{25}$$

where  $q$  is a conservative variable,  $f(q) = aq$  is a flux function, and  $a$  is a characteristic speed. It is well known that the numerical flux, which is calculated by an approximated Riemann solver, can be written in a canonical form as,

$$f^{\text{Riemann}}(q_L, q_R) = \frac{1}{2}(f(q_L) + f(q_R)) - \frac{|a|}{2}(q_R - q_L). \tag{26}$$

As in (26), the numerical flux consists of the consistent term (the first term) and the artificial viscosity term (the second term). Although the artificial viscosity term helps avoid the numerical oscillation error near the discontinuous solution, this term often works excessively and smears the numerical solution non-physically. To suppress the excessive numerical dissipation error, the value of  $|q_R - q_L|$  in the artificial viscosity term should be decreased. The difference between the left- and right cell-boundary values  $|q_R - q_L|$  is here defined as Boundary Variation (BV), and the idea that the value of BV should be diminishing was proposed as Boundary Variation Diminishing (BVD) principle [27].

We introduce two hybrid-type BVD schemes that have multiple candidate reconstruction functions. The first one is the MUSCL-THINC-BVD scheme [28], which contains the MUSCL scheme and the THINC scheme as the candidate reconstruction functions. Another one is the Adaptive THINC-BVD scheme [29], which contains two THINC schemes with different gradient parameters. These hybrid-type BVD schemes select one candidate interpolant for each computational cell based on the BVD principle. The details of the MUSCL scheme and the THINC scheme with the BVD selection algorithm are described below.

#### 3.2.2. Candidate reconstruction function 1: MUSCL scheme

The MUSCL scheme [20] is one of the mainstream shock-capturing numerical methods in the compressible flow simulations. The MUSCL scheme adopts piecewise-linear interpolation and limits the gradient of the reconstruction function so that both the second-order accuracy and the TVD condition [26] are satisfied. For its simplicity and robustness, the MUSCL scheme has been used in various applications.

The cell-boundary values interpolated by the MUSCL scheme are expressed as,

$$\left\{ \begin{array}{l} q_{L,i+\frac{1}{2}}^{\text{MUSCL}} = Q_i^{\text{MUSCL}}\left(x_{i+\frac{1}{2}}\right) \\ \quad = \bar{q}_i + \frac{1}{2}\Phi\left(r_{L,i+\frac{1}{2}}\right)(\bar{q}_{i+1} - \bar{q}_i), \\ q_{R,i-\frac{1}{2}}^{\text{MUSCL}} = Q_i^{\text{MUSCL}}\left(x_{i-\frac{1}{2}}\right) \\ \quad = \bar{q}_i - \frac{1}{2}\Phi\left(r_{R,i-\frac{1}{2}}\right)(\bar{q}_i - \bar{q}_{i-1}), \end{array} \right. \tag{27}$$

where  $\Phi(r)$  is the slope limiter function of the slope ratio  $r_{L,i+\frac{1}{2}} = \frac{\bar{q}_{i+1}-\bar{q}_i}{\bar{q}_i-\bar{q}_{i-1}}$ , or  $r_{R,i-\frac{1}{2}} = \frac{\bar{q}_i-\bar{q}_{i-1}}{\bar{q}_{i+1}-\bar{q}_i}$ . We adopt the following limiter function that is called ‘‘van Leer limiter’’ [50],

$$\Phi_{\text{vanLeer}}(r) = \frac{r + |r|}{1 + |r|}. \tag{28}$$

The MUSCL scheme has second-order accuracy for the smooth solutions and avoids numerical oscillation errors near the discontinuous solutions by introducing a non-linear limiter such as the slope limiter  $\Phi(r)$ . However, it is well-known that such a non-linear limiter often produces excessive numerical dissipation error, resulting in non-physical diffusion of discontinuous solutions. To address this issue, we also utilize another type of reconstruction method.

### 3.2.3. Candidate reconstruction function 2: THINC scheme

The THINC scheme [38,39] was originally developed as a moving-interface capturing method. The THINC reconstruction function has a step-like shape that mimics the discontinuous solution. Recently, the general adaptability of the THINC scheme to the discontinuous solution has extended it to the compressible flow simulation [27–33,35,51–54] for capturing the shock waves, contact discontinuities, and two-phase interfaces. We describe the symmetry-preserving formulation of the THINC scheme [51,54], which is mathematically equivalent to the original formulation, but can strictly preserve the spatial-symmetry property of the numerical solution (see Appendix A).

If the numerical solution satisfies the local monotonicity condition:  $(\bar{q}_{i+1} - \bar{q}_i)(\bar{q}_i - \bar{q}_{i-1}) > 10^{-20}$ , the step-like reconstruction function in the THINC scheme can be determined as [51],

$$Q_i^{\text{THINC}}(x) = q_{a,i} + q_{d,i} \tanh(\beta(X_i(x) - d_i)), \tag{29}$$

where

$$q_{a,i} = \frac{\bar{q}_{i-1} + \bar{q}_{i+1}}{2}, \quad q_{d,i} = \frac{\bar{q}_{i+1} - \bar{q}_{i-1}}{2}, \quad X_i(x) = \frac{x - x_i}{\Delta x}. \tag{30}$$

The parameter  $d_i$  in (29) indicates the location of the jump center of the reconstruction function, and is determined so that the reconstruction function satisfies the conservative condition:

$$\frac{1}{\Delta x} \int_{x_{i-\frac{1}{2}}}^{x_{i+\frac{1}{2}}} Q_i^{\text{THINC}}(x) dx = \bar{q}_i. \tag{31}$$

Solving (31), we can derive  $d_i$  as,

$$d_i = \frac{1}{2\beta} \ln \frac{1 - \mathcal{T}_{2,i}/\mathcal{T}_1}{1 + \mathcal{T}_{2,i}/\mathcal{T}_1}, \tag{32}$$

where

$$\mathcal{T}_1 = \tanh\left(\frac{\beta}{2}\right), \quad \mathcal{T}_{2,i} = \tanh\left(\frac{\beta}{2} \frac{\bar{q}_i - q_{a,i}}{q_{d,i}}\right). \tag{33}$$

Substituting (32) into (29), the cell-boundary values can be obtained as,

$$\left\{ \begin{aligned} q_{L,i+\frac{1}{2}}^{\text{THINC}} &= Q_i^{\text{THINC}}\left(x_{i+\frac{1}{2}}\right) \\ &= q_{a,i} + q_{d,i} \frac{\mathcal{T}_1 + \mathcal{T}_{2,i}/\mathcal{T}_1}{1 + \mathcal{T}_{2,i}}, \\ q_{R,i-\frac{1}{2}}^{\text{THINC}} &= Q_i^{\text{THINC}}\left(x_{i-\frac{1}{2}}\right) \\ &= q_{a,i} - q_{d,i} \frac{\mathcal{T}_1 - \mathcal{T}_{2,i}/\mathcal{T}_1}{1 - \mathcal{T}_{2,i}}. \end{aligned} \right. \tag{34}$$

If the solution is locally non-monotonic, as the step-like reconstruction function (29) cannot be determined, the THINC scheme offers piecewise constant interpolation, i.e.,  $Q_i^{\text{THINC}}(x) = \bar{q}_i$ .

The only undetermined parameter in (29) is  $\beta$ , which represents a gradient of the THINC reconstruction function. The THINC function becomes more discontinuous as the value of  $\beta$  increases, while it becomes smoother as the value of  $\beta$  decreases. It has been reported [29,30,32] that when  $\beta$  has a small value like 1.1, the THINC scheme exhibits characteristics equivalent to the MUSCL scheme with the van Leer limiter. The THINC scheme with  $\beta = \ln(3.0)$  ( $\approx 1.0986$ ) has analytically second-order accuracy [55]. On the other hand, when the value of  $\beta$  is large, such as 1.6 to 2.0, the THINC scheme can resolve discontinuous solutions with a width of approximately 3 to 4 cells. In other words, depending on the value of  $\beta$ , the characteristics of the THINC scheme differ: it excels in interpolating smooth solutions when  $\beta$  is small and in interpolating discontinuous solutions when  $\beta$  is large. In this paper, we denote

THINC with a small  $\beta$  as THINC( $\beta_s$ ) and THINC with a large  $\beta$  as THINC( $\beta_l$ ) for brevity. The value of  $\beta$  is set as 1.1 in the THINC( $\beta_s$ ), and 1.6 in the THINC( $\beta_l$ ).

For computational efficiency, we note that if the value of  $\beta$  is independent of space and time, the value of  $\mathcal{T}_1$  in (33) can be pre-calculated and is not necessarily calculated in each computational cell and time step.

### 3.2.4. BVD selection algorithm

As stated in section 3.2.1, we introduce the hybrid-type BVD schemes that select an appropriate reconstruction function among the candidate interpolants according to the BVD principle. The MUSCL-THINC-BVD scheme has the MUSCL and THINC( $\beta_l$ ) schemes, and the Adaptive THINC-BVD scheme has the THINC( $\beta_s$ ) and THINC( $\beta_l$ ) schemes as the candidate interpolants, respectively. These BVD schemes select one candidate interpolant for each cell following the BVD selection algorithm proposed in [28,34]. We describe the detail of the BVD selection algorithm among numerical schemes “A” and “B” below.

The BVD selection algorithm has two steps. The first step is to compute the values of minimum total boundary variation (mTBV) for both schemes “A” and “B”, which is defined as,

$$mTBV_i^\xi \equiv \min \left( \left| q_{L,i-\frac{1}{2}}^A - q_{R,i-\frac{1}{2}}^\xi \right| + \left| q_{L,i+\frac{1}{2}}^\xi - q_{R,i+\frac{1}{2}}^A \right|, \right. \\ \left| q_{L,i-\frac{1}{2}}^A - q_{R,i-\frac{1}{2}}^\xi \right| + \left| q_{L,i+\frac{1}{2}}^\xi - q_{R,i+\frac{1}{2}}^B \right|, \\ \left| q_{L,i-\frac{1}{2}}^B - q_{R,i-\frac{1}{2}}^\xi \right| + \left| q_{L,i+\frac{1}{2}}^\xi - q_{R,i+\frac{1}{2}}^A \right|, \\ \left. \left| q_{L,i-\frac{1}{2}}^B - q_{R,i-\frac{1}{2}}^\xi \right| + \left| q_{L,i+\frac{1}{2}}^\xi - q_{R,i+\frac{1}{2}}^B \right| \right), \tag{35}$$

for  $\xi = A$  and  $B$ . The second step is to compare the values of  $mTBV_i^A$  and  $mTBV_i^B$ , and determine a reconstruction function whose value of the  $mTBV_i$  is small,

$$Q_i(x) = \begin{cases} Q_i^A(x), & \text{if } mTBV_i^A < mTBV_i^B, \\ Q_i^B(x), & \text{otherwise.} \end{cases} \tag{36}$$

This selection algorithm can be reasonable to perform the high-fidelity reconstruction because the numerical scheme which gives smaller value of  $mTBV_i$  can reduce the value of  $|q_R - q_L|$  in the numerical flux (26), resulting in decreases of the numerical dissipation and anti-dissipation errors. The MUSCL-THINC-BVD scheme sets the numerical scheme “A” as MUSCL and “B” as THINC( $\beta_l$ ) schemes. The Adaptive THINC-BVD scheme sets “A” as THINC( $\beta_s$ ) and “B” as THINC( $\beta_l$ ) schemes.

The reconstruction is conducted on quasi-primitive variables  $q^{qp} = (\alpha_1, \alpha_1 \rho_1, \alpha_2 \rho_2, \mathbf{u}, p)^T$ . Replacement of the reconstruction function to the THINC( $\beta_l$ ) according to the BVD selection procedure is conducted for the variables  $\alpha_1$ ,  $\alpha_1 \rho_1$ , and  $\alpha_2 \rho_2$ , whose values vary in gas/vapor-liquid interfaces and contact discontinuities. In other words, for  $\mathbf{u}$  and  $p$ , the reconstruction function is fixed to MUSCL in the MUSCL-THINC-BVD scheme and THINC( $\beta_s$ ) in the Adaptive THINC-BVD scheme.

### 3.3. Wave-propagation method

After obtaining the cell-boundary values by the reconstruction, the spatial discretization is performed by the wave-propagation method [56,57]. The wave-propagation method is often adopted for its efficiency in dealing with non-conservative terms in hyperbolic equations [18,28,46,56,58,59]. The formulation proposed in [57] allows for more varied reconstruction methods, such as higher than second-order schemes or the THINC scheme. In that formulation, the spatial discretization is performed as,

$$\frac{d\bar{q}_i}{dt} = -\frac{1}{\Delta x} (\mathcal{A}^+ \Delta Q_{i-\frac{1}{2}} + \mathcal{A}^- \Delta Q_{i+\frac{1}{2}} + \mathcal{A} \Delta Q_i), \tag{37}$$

where  $\mathcal{A}^\pm \Delta Q_{i\pm\frac{1}{2}}$  indicates so-called fluctuations at cell boundary  $x = x_{i\pm\frac{1}{2}}$ .  $\mathcal{A}^+ \Delta Q_{i+\frac{1}{2}}$  and  $\mathcal{A}^- \Delta Q_{i+\frac{1}{2}}$  are right-going and left-going fluctuations respectively, and  $\mathcal{A} \Delta Q_i$  is a total fluctuation between cell boundaries  $x = x_{i-\frac{1}{2}}$  and  $x_{i+\frac{1}{2}}$ . These fluctuations are calculated by solving local Riemann problems;  $\mathcal{A}^\pm \Delta Q_{i\pm\frac{1}{2}}$  is obtained from the cell-boundary values  $q_{L,i\pm\frac{1}{2}}$  and  $q_{R,i\pm\frac{1}{2}}$ , and  $\mathcal{A} \Delta Q_i$  is obtained from  $q_{R,i-\frac{1}{2}}$  and  $q_{L,i+\frac{1}{2}}$  [57,59].

To calculate the values of the fluctuations, we introduce the Harten-Lax-van Leer-Contact (HLLC) [60] Riemann solver. The HLLC solver defines a Riemann solution structure by a set of 3 waves  $\mathcal{W}^l$  and corresponding speeds  $S^l$ ,  $l = 1, 2, 3$ , as,

$$S^1 = S_L, \quad S^2 = S_\star, \quad S^3 = S_R, \tag{38}$$

$$\mathcal{W}^1 = q_{\star L} - q_L, \quad \mathcal{W}^2 = q_{\star R} - q_{\star L}, \quad \mathcal{W}^3 = q_R - q_{\star R}, \tag{39}$$

that separate four constant states  $q_L$ ,  $q_{*L}$ ,  $q_{*R}$  and  $q_R$ . Here, the quantities corresponding to the states  $q_{*L}$  and  $q_{*R}$  adjacent (to the left and right, respectively) to the medium wave propagating at speed  $S_*$  are denoted by subscripts  $\star L$  and  $\star R$ . The left and right wave speeds  $S_L$  and  $S_R$  are estimated as,

$$S_L = \min(u_L - c_L, u_R - c_R), \quad S_R = \max(u_L + c_L, u_R + c_R). \tag{40}$$

Then, the speed  $S_*$  is determined as,

$$S_* = \frac{(\rho_L - \rho_R) + (\rho_L u_L (S_L - u_L) - \rho_R u_R (S_R - u_R))}{\rho_L (S_L - u_L) - \rho_R (S_R - u_R)}. \tag{41}$$

The middle states  $q_{*L}$  and  $q_{*R}$  are determined so as to satisfy the Rankine-Hugoniot conditions for each wave, as,

$$q_{\star K} = \begin{bmatrix} \alpha_{1,K} \\ (\alpha_1 \rho_1)_K \chi_K \\ (\alpha_2 \rho_2)_K \chi_K \\ \rho_K S_* \chi_K \\ (\alpha_1 \rho_1)_K \chi_K \left( \frac{E_{1,K}}{\rho_{1,K}} + (S_* - u_K) \left( S_* + \frac{p_K}{\rho_{1,K}(S_K - u_K)} \right) \right) \\ (\alpha_2 \rho_2)_K \chi_K \left( \frac{E_{2,K}}{\rho_{2,K}} + (S_* - u_K) \left( S_* + \frac{p_K}{\rho_{2,K}(S_K - u_K)} \right) \right) \end{bmatrix}, \tag{42}$$

for  $K = L$  and  $R$ , where  $\chi_K = \frac{S_K - u_K}{S_K - S_*}$ . Then, the fluctuations are calculated as,

$$\mathcal{A}^\pm \Delta Q_{i+\frac{1}{2}} = \sum_{l=1}^3 \left( S_{i+\frac{1}{2}}^l \right)^\pm \mathcal{W}_{i+\frac{1}{2}}^l. \tag{43}$$

Here,  $(S)^\pm = \frac{1}{2}(S \pm |S|)$  splits the fluctuations into positive- and negative-direction.

The total fluctuation  $\mathcal{A} \Delta Q_i$  between cell boundaries  $x = x_{i-\frac{1}{2}}$  and  $x_{i+\frac{1}{2}}$  is calculated similarly to  $\mathcal{A}^\pm \Delta Q_{i+\frac{1}{2}}$ . The  $\mathcal{A} \Delta Q_i$  is calculated as,

$$\mathcal{A} \Delta Q_i = \sum_{l=1}^3 S_i^l \mathcal{W}_i^l, \tag{44}$$

where  $\mathcal{W}_i^l$  and  $S_i^l$  are a  $l$ -th wave and a corresponding speed respectively which come from a Riemann solution structure based on the cell-boundary values  $q_{R,i-\frac{1}{2}}$  and  $q_{L,i+\frac{1}{2}}$ . In other words, a Riemann problem arising from a data set  $\{q_{R,i-\frac{1}{2}}, q_{L,i+\frac{1}{2}}\}$  is solved, and then each wave  $\mathcal{W}_i^l$  and corresponding speed  $S_i^l$  add up as (44) without splitting.

After obtaining the fluctuations  $\mathcal{A}^+ \Delta Q_{i-\frac{1}{2}}$ ,  $\mathcal{A}^- \Delta Q_{i+\frac{1}{2}}$ , and  $\mathcal{A} \Delta Q_i$ , the time-derivative of the numerical solution  $\frac{dq_i}{dt}$  is calculated from (37), and the time-evolution is conducted by the 3rd-order Runge-Kutta method [49].

### 3.4. Relaxation method

The numerical solution obtained after the time evolution of a homogeneous part of the six-equation model is in non-equilibrium states for pressure, temperature, and Gibbs energy. In this section, the relaxation methods to reach the equilibrium states are described. Assuming the mechanical relaxation characteristic time  $1/\mu$  is much smaller than the thermal and chemical relaxation characteristic times  $1/\theta$  and  $1/\nu$  [18], the pressure relaxation equation is firstly solved. Each operation of solving mechanical, thermal, and chemical relaxation is denoted as  $\mathcal{L}_p$ ,  $\mathcal{L}_{pT}$ , and  $\mathcal{L}_{pTg}$ , respectively. These operations are corresponding to solving the source terms  $\psi_p(q)$ ,  $\psi_p(q) + \psi_T(q)$ , and  $\psi_p(q) + \psi_T(q) + \psi_g(q)$  in (14) and (15).

As discussed in [18], the possible patterns of the relaxation methods in terms of the complete solutions are shown as,

$$q^{n+1} = \mathcal{L}_p \mathcal{L}_{hyp}^{\Delta t} q^n, \quad (\text{p-relaxation}), \tag{45a}$$

$$q^{n+1} = \mathcal{L}_{pT} \mathcal{L}_p \mathcal{L}_{hyp}^{\Delta t} q^n, \quad (\text{p-pT-relaxation}), \tag{45b}$$

$$q^{n+1} = \mathcal{L}_{pTg} \mathcal{L}_p \mathcal{L}_{hyp}^{\Delta t} q^n, \quad (\text{p-pTg-relaxation}), \tag{45c}$$

$$q^{n+1} = \mathcal{L}_{pTg} \mathcal{L}_{pT} \mathcal{L}_p \mathcal{L}_{hyp}^{\Delta t} q^n, \quad (\text{p-pT-pTg-relaxation}). \tag{45d}$$

The p-relaxation (45a) method conducts the pressure relaxation but does not consider the heat and mass transfer. The p-pT-relaxation (45b) method conducts the pressure and temperature relaxation but does not perform the mass transfer. The numerical solutions of the p-relaxation (45a) and p-pT-relaxation methods (45b) are non-equilibrium for Gibbs energy, thus the phase change is not simulated. On the other hand, the numerical solutions of the p-pTg-relaxation (45c) and p-pT-pTg-relaxation (45d) methods reach an equilibrium state for Gibbs energy, and a part of the liquid phase is changed to be gas phase under metastable condition. The relaxation rates for pressure, temperature, and Gibbs energy are assumed to be infinite:  $\mu, \theta, \nu \rightarrow \infty$ , hence the equilibrium states can

be obtained by simple algebraic operations without any ODE solvers. The calculation procedures of the operations  $\mathcal{L}_p$ ,  $\mathcal{L}_{pT}$ , and  $\mathcal{L}_{pTg}$  and their derivations are given in Appendix B, Appendix C, and Appendix D, respectively.

### 3.5. Overall calculation procedure

We summarize the overall calculation procedure as follows.

(I) Perform the spatial reconstruction on the quasi-primitive variables  $q^{qp} = (\alpha_1, \alpha_1 \rho_1, \alpha_2 \rho_2, u, p)^T$  and calculate the cell-boundary values  $q^{qp}_{L,i+\frac{1}{2}}$  and  $q^{qp}_{R,i-\frac{1}{2}}$ . The calculation procedure of the MUSCL-THINC-BVD scheme is briefly described below as an example.

- i) Calculate the cell-boundary values  $q^\xi_{L,i+\frac{1}{2}}$  and  $q^\xi_{R,i-\frac{1}{2}}$  where  $\xi = \text{MUSCL}$  and  $\text{THINC}(\beta_l)$ . The details of the MUSCL and THINC schemes are in section 3.2.2 and section 3.2.3, respectively.
- ii) Calculate the value of  $mTBV_i^\xi$  in (35) for each scheme, using the cell-boundary values  $q^\xi_{L,i+\frac{1}{2}}$  and  $q^\xi_{R,i-\frac{1}{2}}$ .
- iii) Comparing the values of  $mTBV_i^{\text{MUSCL}}$  and  $mTBV_i^{\text{THINC}(\beta_l)}$ , select the final reconstruction function that gives smaller value of  $mTBV_i$ , as (36).

In the case of the Adaptive THINC-BVD scheme, the MUSCL scheme is replaced by the  $\text{THINC}(\beta_s)$  scheme.

- (II) Using the wave-propagation method, obtain the time derivative of the numerical solutions  $\frac{dq_i}{dt}$  as (37). The detail is described in section 3.3.
- (III) Time evolution is conducted using the 3rd-order Runge-Kutta method [49]. Now the operation  $\mathcal{L}_{\text{hyp}}^{\Delta t}$  is finished.
- (IV) Solve the relaxation equation in (45) and update the variables to achieve the equilibrium state.

In this calculation procedure, the spatial symmetry of the numerical solution can be completely preserved by carefully executing certain calculations. Special attention is needed for the THINC formulation in the step (I)-i) and the wave-propagation method in the step (II). The details on the symmetry preservation are explained in Appendix A.

## 4. Numerical results

To demonstrate the high fidelity of the proposed schemes, some typical benchmark tests are solved. The numerical results of the MUSCL-THINC-BVD and the Adaptive THINC-BVD schemes are compared to those of the MUSCL scheme. The CFL number is set to 0.5 in all benchmark tests.

### 4.1. 1D water-cavitation tube problem

In this test, two rarefaction waves moving outward are simulated. The computational domain ( $x \in [0, 1 \text{ m}]$ ) is initially filled with liquid of water ( $\alpha_1 = 0.99$ ). The SGEOS parameters for this test are shown in Table 1. With pressure reduction at the center of the computational domain, the cavitation can be simulated. The initial pressure is  $10^5 \text{ Pa}$  around the atmospheric pressure, and the gas density is  $\rho_2 = 1150 \text{ kg/m}^3$ . Then, using isothermal condition,  $T_1 = T_2 = 354.728 \text{ K}$  and  $\rho_2 = 0.63 \text{ kg/m}^3$  are obtained. Denoting the speed of the two rarefaction waves moving in opposite directions as  $|u_0| \text{ [m/s]}$ , the initial condition is summarized as,

$$(\alpha_1, \rho_1 \text{ [kg/m}^3\text{]}, \rho_2 \text{ [kg/m}^3\text{]}, u \text{ [m/s]}, p \text{ [Pa]})_{t=0} = \begin{cases} (0.99, 1150, 0.63, -|u_0|, 10^5) & \text{for } 0 \text{ m} < x < 0.5 \text{ m,} \\ (0.99, 1150, 0.63, |u_0|, 10^5) & \text{for } 0.5 \text{ m} < x < 1 \text{ m.} \end{cases} \quad (46)$$

The boundary condition is set as the outflow condition. Two values of the initial velocity,  $|u_0| = 2 \text{ m/s}$  and  $|u_0| = 500 \text{ m/s}$  are tested. The mesh number is set to 500 for the  $|u_0| = 2 \text{ m/s}$  test and 5000 for  $|u_0| = 500 \text{ m/s}$  test. To address the strong rarefaction waves, for the problem with  $|u_0| = 500 \text{ m/s}$ , we add the condition  $\nabla \cdot \mathbf{u} < 0$  (i.e., compressional waves) for selecting the  $\text{THINC}(\beta_l)$  function as the BVD admissible interpolation function.

The numerical results with four-type relaxation methods in (45), namely p-relaxation (red circle marker and solid line), p-pT-relaxation (blue square marker and dashed line), p-pTg-relaxation (green triangle marker and dotted line), and p-pT-pTg-relaxation (orange cross marker and dash-dot line), are shown in Figs. 1 ( $|u_0| = 2 \text{ m/s}$ ) and 2 ( $|u_0| = 500 \text{ m/s}$ ). The results of the four-type relaxation methods are in general agreement with the results in [18]. It is important to emphasize here that the results of MUSCL and Adaptive THINC-BVD schemes show generally similar solution structures. From these results, it can be seen that the Adaptive THINC-BVD scheme appropriately selects the  $\text{THINC}(\beta_s)$  at smooth rarefaction waves. We omitted the numerical results for the MUSCL-THINC-BVD scheme since they are almost the same as those for the MUSCL scheme. For example, in the distribution of mass fraction, the difference between the numerical results of MUSCL and MUSCL-THINC-BVD is negligible, with a maximum of  $1.49 \times 10^{-6}$  at  $|u_0| = 2 \text{ m/s}$  and a maximum of  $6.00 \times 10^{-5}$  at  $|u_0| = 500 \text{ m/s}$ .

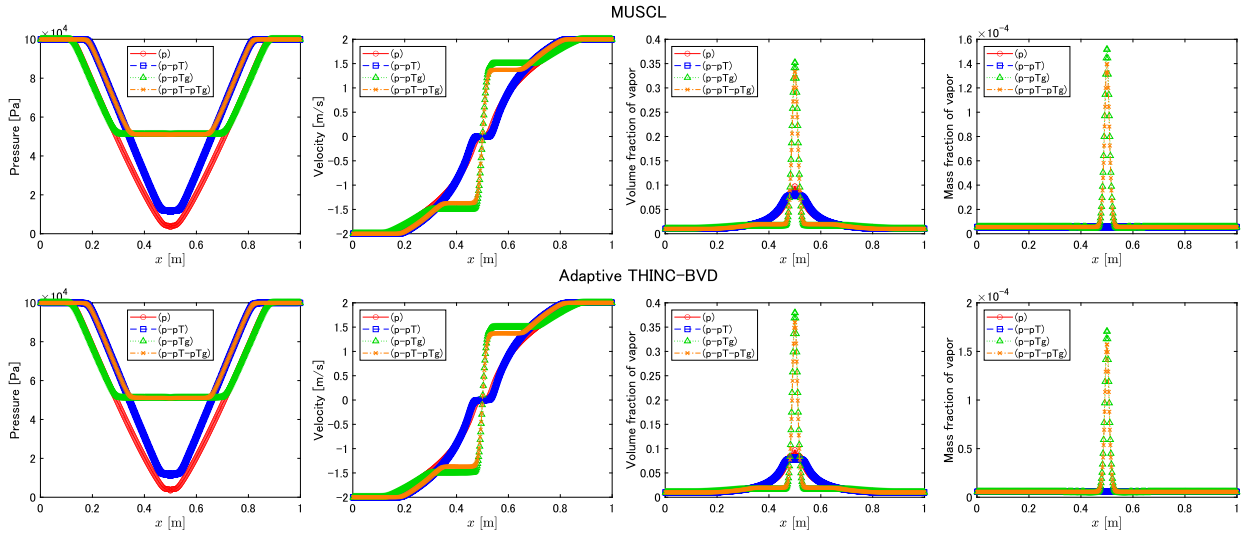


Fig. 1. Numerical results of pressure, velocity, volume fraction, and mass fraction of vapor at  $t = 3.2$  ms in 1D water-cavitation tube problem with  $|u_0| = 2$  m/s. The top and bottom rows show the numerical results of MUSCL and Adaptive THINC-BVD schemes respectively. (For interpretation of the colors in the figure(s), the reader is referred to the web version of this article.)

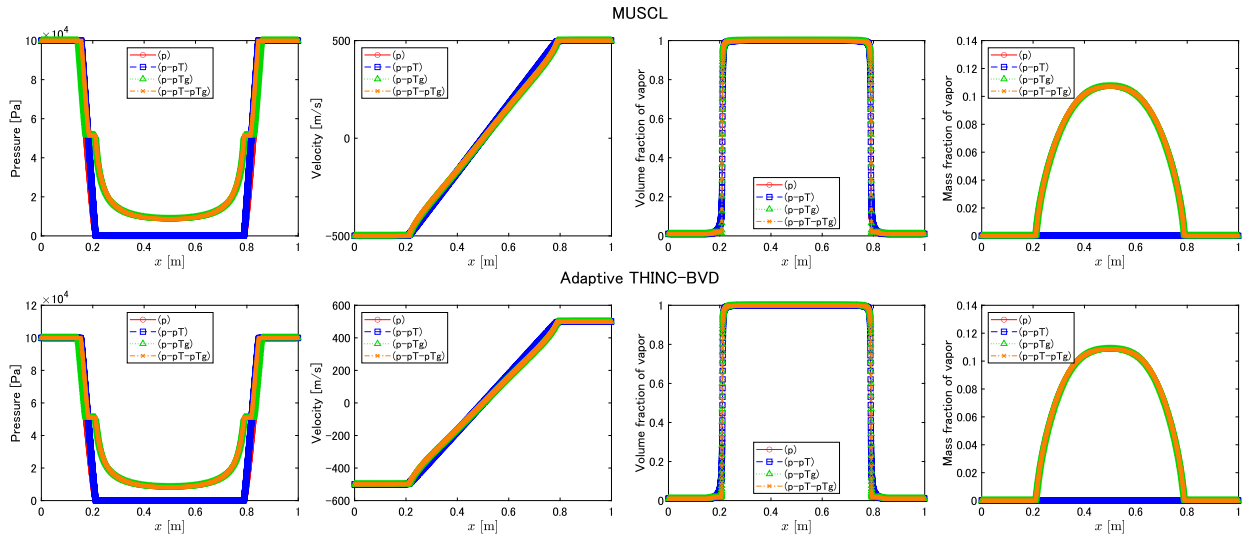


Fig. 2. Numerical results of pressure, velocity, volume fraction, and mass fraction of vapor at  $t = 0.58$  ms in 1D water-cavitation tube problem with  $|u_0| = 500$  m/s. The top and bottom rows show the numerical results of MUSCL and Adaptive THINC-BVD schemes respectively.

#### 4.2. 1D water shock tube problem with a mixture containing mainly water vapor

This shock tube problem was proposed in terms of the four-equation model in [61], and here we solve this problem with the six-equation model. The computational domain is  $x \in [0, 1]$  m. The SGEOS parameters for this test are shown in Table 1. The initial pressure is  $2 \times 10^5$  Pa on the left side of the computational domain, and  $10^5$  Pa on the right side. The mass fraction of liquid is entirely set to 0.2, and the velocity is 0 m/s. The temperature is set to be the saturation temperature at the given pressure, namely  $T_1 = T_2 = 394.25$  K on the left side and  $T_1 = T_2 = 372.88$  K on the right side. From this condition, the initial condition in terms of the primitive variables can be derived as,

$$\begin{aligned}
 & (\alpha_1, \rho_1 [\text{kg/m}^3], \rho_2 [\text{kg/m}^3], u [\text{m/s}], p [\text{Pa}])_{t=0} = \\
 & \begin{cases} (2.7399 \times 10^{-4}, 1034.8, 1.1344, 0, 2 \times 10^5) & \text{for } 0 < x < 0.5 \text{ m,} \\ (1.3702 \times 10^{-4}, 1094.0, 0.59969, 0, 10^5) & \text{for } 0.5 \text{ m} < x < 1 \text{ m.} \end{cases} \quad (47)
 \end{aligned}$$

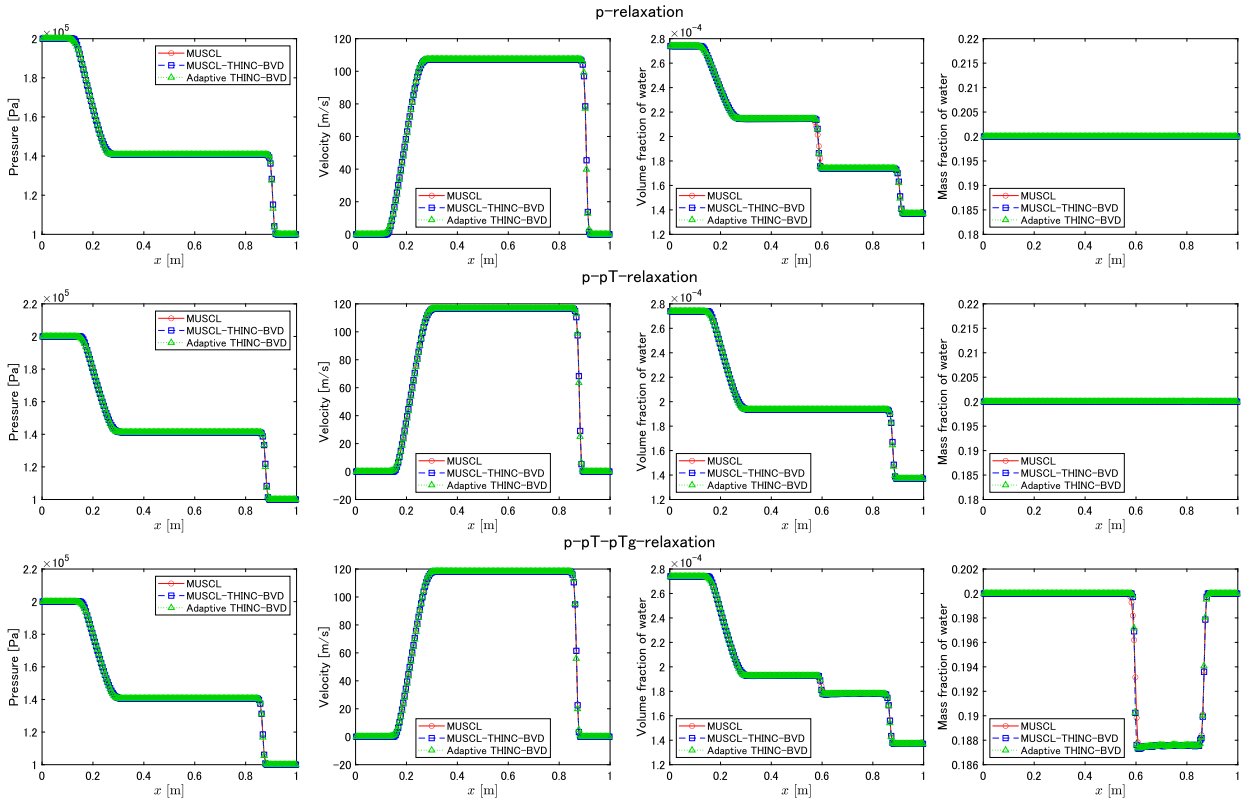


Fig. 3. Numerical results of pressure, velocity, volume fraction, and mass fraction of water at  $t = 0.8$  ms in 1D water shock-tube problem with a mixture containing mainly water vapor. The top, middle, and bottom panels show the results of p-relaxation, p-pT-relaxation (without phase change), and p-pT-pTg-relaxation (with phase change) respectively.

The boundary condition is set as the outflow condition. The mesh number is 200 with the cell size  $\Delta x = 0.005$  m. For the relaxation method, p-relaxation and p-pT-relaxation are used for no phase change, and p-pT-pTg-relaxation is used for phase change simulation.

The numerical results are shown in Fig. 3. The results of p-pT-relaxation (without phase change) agree well with the results in [61], since the four-equation model in [61] assumes pressure and temperature equilibrium. The results of p-pT-pTg-relaxation (with phase change) are also reasonable compared to the results in [61], considering that the numerical model does not deal with condensation but only with evaporation.

The advantage of the BVD reconstruction schemes is observed in this test. Focusing on the contact discontinuity at  $x \approx 0.6$  m in plots of the volume fraction and mass fraction of water, we can see that the BVD schemes captured the discontinuity within approximately 3 to 4 cells, however, the MUSCL scheme needed more number of cells. Such high-resolution results indicate that the BVD schemes properly select the THINC function with large  $\beta$  near the discontinuities and have superiority over the existing scheme in terms of discontinuity-capturing performance.

### 4.3. 2D cavitating Richtmyer-Meshkov instability (RMI) problem

This benchmark test is conducted to check the performances of the numerical schemes in a multi-dimensional case. When the reflected shock wave passes through the gas/vapor-liquid interface, the Richtmyer-Meshkov instability (RMI) occurs, leading to the observation of mushroom-shaped flow structures. This test was introduced in [8,18], however, the phase change has been neglected. Here, just using the SGEOS parameters for water in Table 1 and keeping other test settings in [8,18], we consider the phase change in this test. To our knowledge, the numerical results with phase change have never been reported.

The computational domain is set as  $x \in [0, 3 \text{ m}] \times y \in [0, 1 \text{ m}]$ . The initial condition is,

$$\begin{aligned}
 & (\alpha_1, \rho_1 [\text{kg/m}^3], \rho_2 [\text{kg/m}^3], u [\text{m/s}], v [\text{m/s}], p [\text{Pa}])_{t=0} = \\
 & \begin{cases} (1 - 10^{-6}, 1000, 100, -200, 0, 10^5) & \text{for } x < 1.2 \text{ m and } r(x, y) > 0.6 \text{ m,} \\ (10^{-6}, 1000, 100, -200, 0, 10^5) & \text{otherwise,} \end{cases} \quad (48)
 \end{aligned}$$

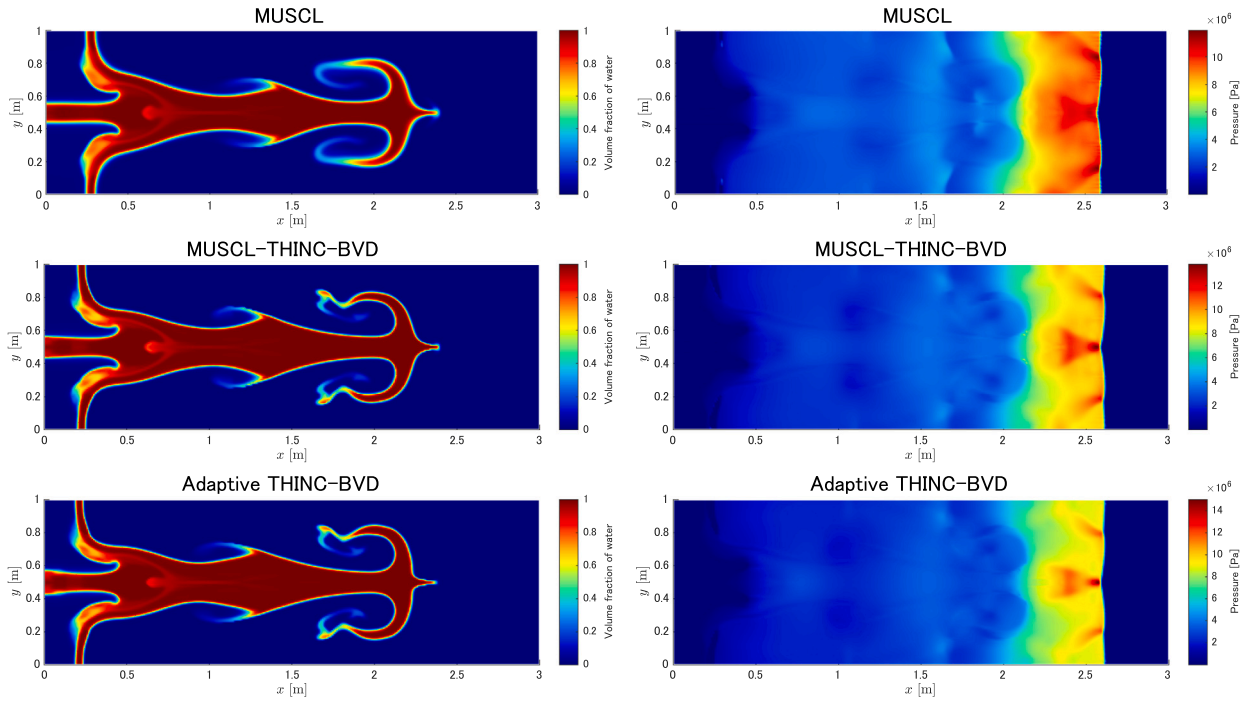


Fig. 4. Pseudo-color plots of the volume fraction of water (left) and pressure (right) at  $t = 10.0$  ms in 2D cavitating Richtmyer-Meshkov instability problem without phase change. The top, middle, and bottom panels show the numerical results of MUSCL, MUSCL-THINC-BVD, and Adaptive THINC-BVD schemes respectively.

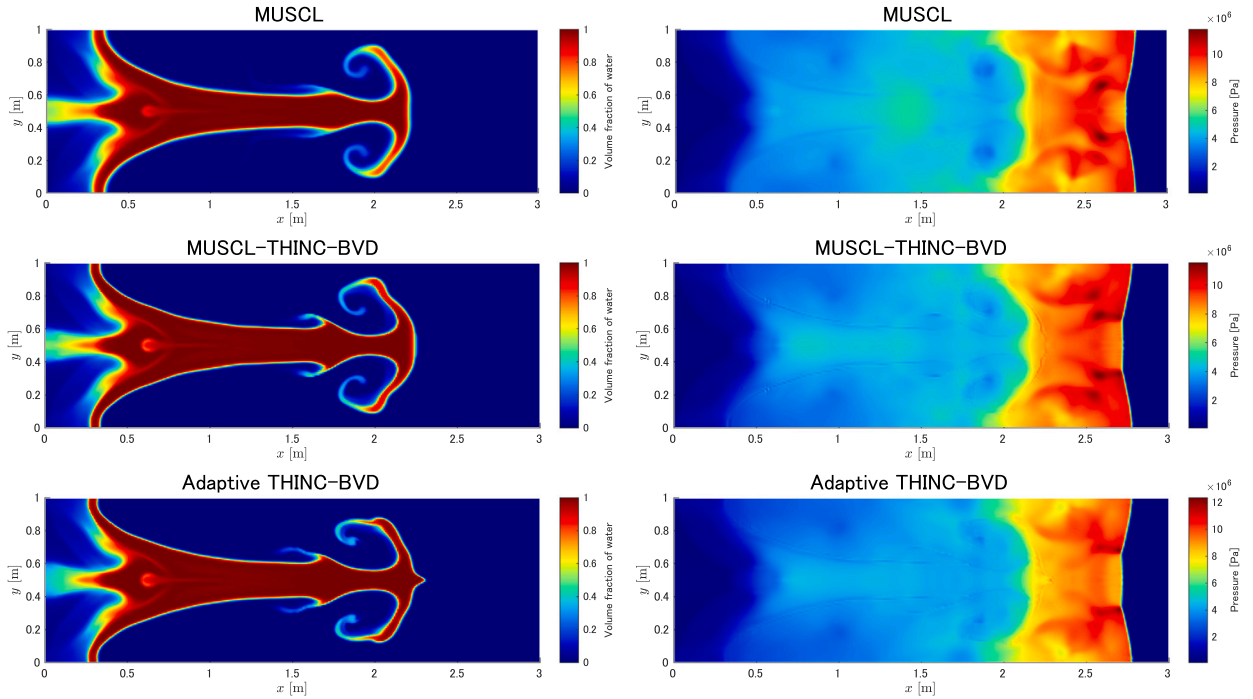


Fig. 5. Same as Fig. 4, but with phase change.

where  $r(x, y) = \sqrt{(x - 1.2)^2 + (y - 0.5)^2}$ . The boundary condition is set as an outflow condition for the right boundary and reflective walls for the other boundaries. The mesh number is  $300 \times 100$  with the cell size  $\Delta x = \Delta y = 0.01$  m. For the relaxation method, p-relaxation is used for no phase change, and p-pT-pTG-relaxation is used for phase change simulation.

The numerical results at  $t = 10.0$  ms of the volume fraction of water and pressure are shown in Figs. 4 and 5. Without phase change (Fig. 4), despite relaxation of pressure only, cavitation pockets are observed near the left wall location in all numerical

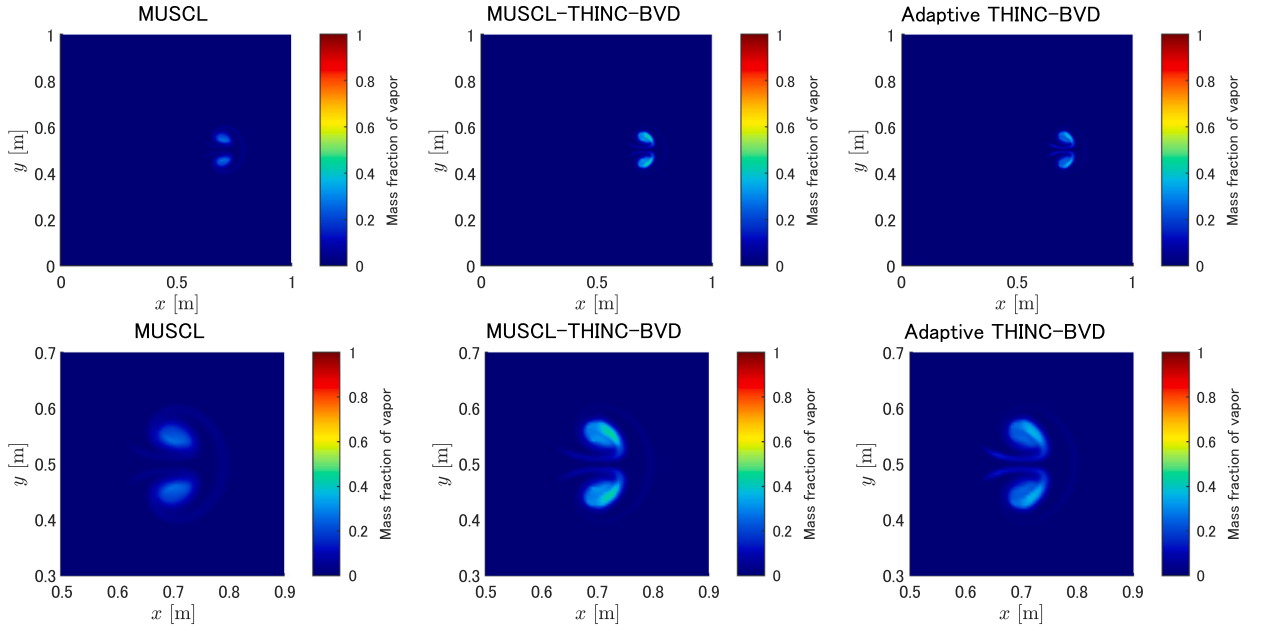


Fig. 6. Pseudo-color plots of the mass fraction of vapor at  $t = 1.4$  ms in 2D vapor-bubble compression problem without phase change. The left, middle, and right panels show the numerical results of MUSCL, MUSCL-THINC-BVD, and Adaptive THINC-BVD schemes respectively. The bottom row shows enlarged views of vapor bubbles.

schemes as in [8,18]. With phase change (Fig. 5), cavitation pockets and instabilities are observed similarly. However, compared to the case without phase change, more vaporization of water is observed near the left wall. The overall flow structures are consistent with the results in [8,18].

Comparing the results of each numerical scheme, the RMI due to shock wave propagation is more significant in the BVD schemes. This difference indicates the lower dissipation errors of the BVD schemes. No significant numerical oscillations are observed in the pressure distribution for all numerical schemes. From these results, it can be concluded that the BVD schemes improve the computational results for both cases with and without phase change.

#### 4.4. 2D vapor-bubble compression problem

In this problem [18,45,62,63], a piston compresses vapor bubble dodecane placed inside liquid dodecane. This problem is used to verify the absence of pressure oscillations and the validity of phase change calculations in multi-dimensional problems. To our knowledge, there are no examples of dynamically generated bubbles due to phase change being captured using existing methods such as the MUSCL scheme.

The computational domain is  $x \in [0, 1 \text{ m}] \times y \in [0, 1 \text{ m}]$ . The SGEOS parameters for the dodecane are shown in Table 2. The initial pressure and temperature are  $10^5$  Pa and 600 K. The radius of the bubble is set to 0.2 m. The bubble and surrounding liquid are approximated as pure phases by their volume fractions of  $1 - 10^{-6}$ . The initial velocity is 0 m/s. Then, the initial condition in terms of the primitive variables can be derived as,

$$\begin{aligned}
 & (\alpha_1, \rho_1 [\text{kg/m}^3], \rho_2 [\text{kg/m}^3], u [\text{m/s}], v [\text{m/s}], p [\text{Pa}])_{t=0} = \\
 & \begin{cases} (1 - 10^{-6}, 458.338, 3.408, 0, 0, 10^5) & \text{for } r(x, y) > 0.2 \text{ m,} \\ (10^{-6}, 458.338, 3.408, 0, 0, 10^5) & \text{otherwise,} \end{cases} \quad (49)
 \end{aligned}$$

where  $r(x, y) = \sqrt{(x - 0.5)^2 + (y - 0.5)^2}$ . The boundary condition is set as a moving reflective wall at constant speed 100 m/s for the left boundary and static reflective walls for the other boundaries. The numerical treatment of the moving wall is referred to [64]. The mesh number is  $200 \times 200$  with the cell size  $\Delta x = \Delta y = 0.005$  m. For the relaxation method, p-relaxation is used for no phase change, and p-PT-pTg-relaxation is used for phase change simulation.

The numerical results of the vapor mass fraction at  $t = 1.4$  ms are shown in Figs. 6 and 7. At  $t = 1.4$  ms, the behavior of vapor bubbles compressed by the piston is observed. Without phase change (Fig. 6), there is no significant difference between the MUSCL scheme and the BVD schemes. On the other hand, with phase change (Fig. 7), a significant difference arises between the MUSCL scheme and the BVD scheme. In the results of the MUSCL scheme, the mass fraction of the compressed vapor is low, while the results of the BVD scheme approach a value close to 1. Considering that this is a calculation taking into account phase change, it is inferred that the results of the BVD schemes reproduce the cavitation phenomenon. This can be attributed to the fact that the BVD scheme used the THINC function with a large  $\beta$  for the interpolation of the vapor-liquid interface, resulting in the suppression of numerical

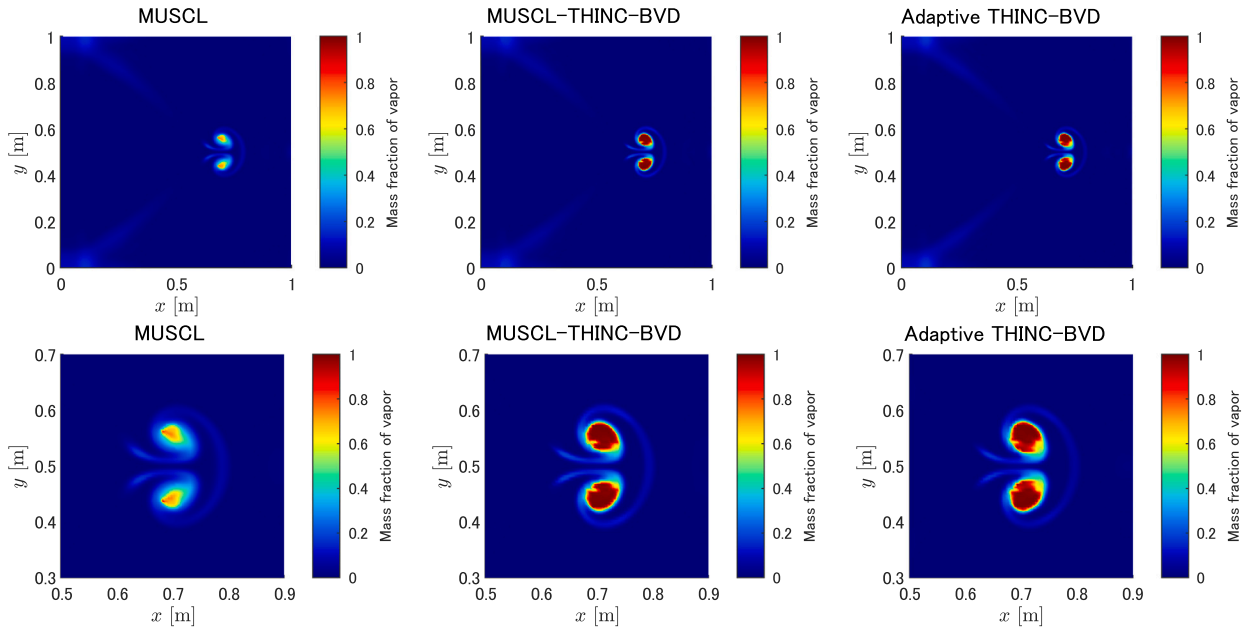


Fig. 7. Same as Fig. 6, but with phase change.

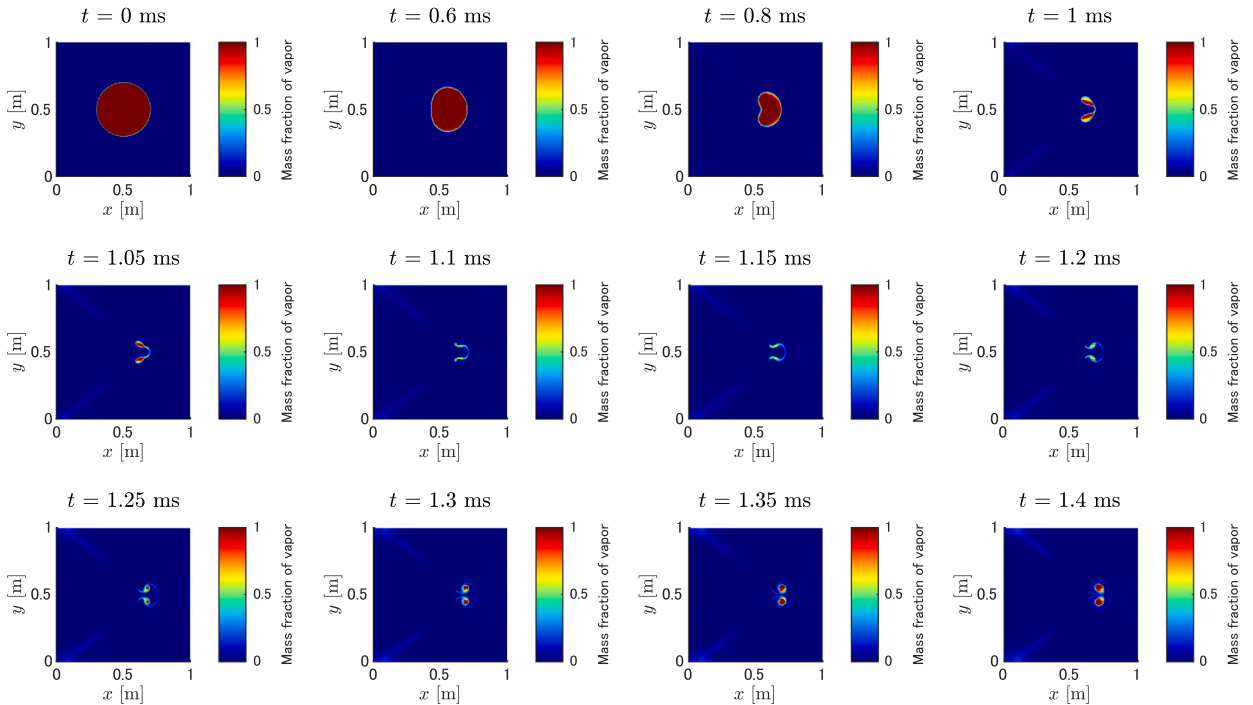


Fig. 8. Pseudo-color plots of the mass fraction of vapor in 2D vapor-bubble compression problem with phase change. The numerical results are computed by the Adaptive THINC-BVD scheme. Time passes from left to right and from top to bottom.

dissipation error. On the other hand, the results of the MUSCL scheme show very small bubble sizes and do not sufficiently reproduce the phase change phenomenon. To achieve results with the MUSCL scheme that are comparable to those obtained with the BVD schemes on a  $200 \times 200$  grid, we increase the grid size to  $400 \times 400$  or  $800 \times 800$  to reach a converged solution, which requires significantly higher computational costs. The numerical results of the BVD schemes that clearly capture dynamically generated vapor-liquid interfaces due to phase change are, to our knowledge, the first of their kind.

Using the time-lapse of the numerical solutions of the vapor bubble compression problem solved with the Adaptive THINC-BVD scheme shown in Figs. 8 and 9, we discuss the mechanism of the dynamic interface generation. From the mass fraction time-lapse

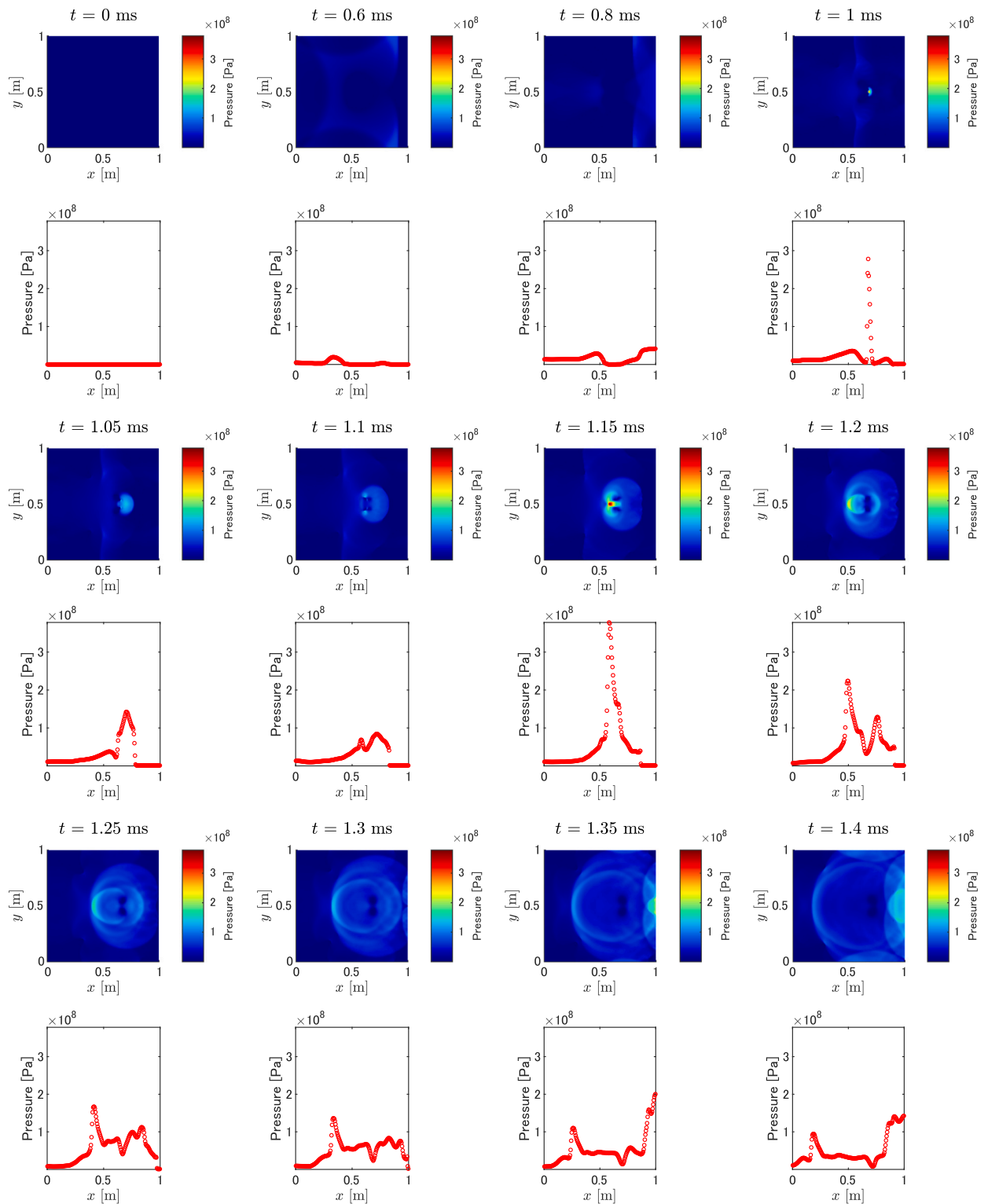


Fig. 9. Pseudo-color plots and 1D distribution in cross-section at  $y = 0.5$  m of the pressure in 2D vapor-bubble compression problem with phase change. The numerical results are computed by the Adaptive THINC-BVD scheme. Time passes from left to right and from top to bottom.

(Fig. 8), it is observed that the bubble is compressed between  $t = 0$  to 1.2 ms, and a new bubble is generated between  $t = 1.2$  to 1.4 ms. Looking at the pressure time-lapse (Fig. 9), large peaks in pressure values are observed at  $t = 1$  ms and 1.15 ms. At  $t = 1$  ms, the pressure peak is considered to be caused by shock waves generated by the piston reflecting on the surrounding walls and concentrating near  $x = 0.7$  m and  $y = 0.5$  m. The subsequent pressure peak at  $t = 1.15$  ms is attributed to interactive shock waves. Meanwhile, two lower-pressure regions are symmetrically generated adjacent to the high-pressure area. These lower pressures continue to develop continuously, falling below the saturation pressure, thus leading to the formation of vapor bubbles, newly created interfaces. This evaporation process is expected in the physical process and should be clearly reproduced in a numerical simulation. See Fig. 7, new interfaces are created between liquid and vapor, which are clearly resolved by the BVD schemes. Conversely, a scheme with higher numerical dissipation, such as the MUSCL scheme as showing above, fails to reproduce a clear interface.

## 5. Conclusion

We proposed low-dissipation numerical schemes for compressible gas/vapor-liquid two-phase flows including phase change phenomena such as cavitation. To suppress numerical dissipation errors in existing schemes, a hybrid approach combining multiple numerical schemes based on the BVD principle was demonstrated. The numerical results from several benchmark tests show that the BVD schemes capture discontinuous solutions with higher resolution compared to a conventional scheme. Particularly, the numerical results capturing dynamically generated gas/vapor-liquid interfaces due to phase change in the 2D vapor-bubble compression problem have not been reported before. The improvements in such numerical results suggest the capability of the BVD schemes to accurately compute both smooth and discontinuous solutions. Thus, the proposed methods are suitable for reproducing interface phenomena such as cavitation in two-phase flow simulations. Although we have focused on the evaporation effects in the chemical relaxation process, the condensation effects are also important and will be an important direction for our future work.

### CRedit authorship contribution statement

**Hiro Wakimura:** Writing – original draft, Visualization, Validation, Software, Resources, Methodology, Investigation, Formal analysis, Data curation, Conceptualization. **Tatsuin Li:** Validation, Software, Methodology. **Keh-Ming Shyue:** Supervision, Software, Methodology. **Takayuki Aoki:** Writing – review & editing, Validation, Supervision, Formal analysis. **Feng Xiao:** Writing – review & editing, Supervision, Project administration, Methodology, Conceptualization.

### Declaration of competing interest

The authors declare that they have no known competing financial interests or personal relationships that could have appeared to influence the work reported in this paper.

### Data availability

No data was used for the research described in the article.

### Acknowledgements

This work was supported in part by the fund from JSPS (Japan Society for the Promotion of Science) under Grant Nos. 18H01366, 19H05613, 22J21252 and 22KJ1331.

The authors would like to give special thanks to Dr. Yoshiaki Abe at Tohoku University and Dr. Takanori Haga at Japan Aerospace Exploration Agency for their inspirational discussions and technical advice.

### Appendix A. Preservation of the spatial symmetry in the flow structures

Flow structures with spatial symmetry are commonly observed (indeed, in all problems in this study except section 4.2), but the preservation methods of this symmetry are not obvious. While some researches [51,65] have been reported on preserving spatial symmetry for single-phase flow using the Euler equations, to our knowledge, no symmetry-preserving methods have been proposed for two-phase flow. Symmetry errors are usually not prominent due to the numerical dissipation errors. However, in the case of low-dissipation schemes, these errors can become significant. Therefore, in this section, based on the proposed schemes, we highlight key points to be considered in preserving symmetry.

Generally, symmetry errors occur in operations involving three or more numbers. In floating-point arithmetic, as shown in the following equations, the introduction of rounding errors depends on the order of operations:

$$(a + b) + c \neq a + (b + c), \quad (\text{A.1})$$

$$(a \times b) \times c \neq a \times (b \times c). \quad (\text{A.2})$$

In other words, when the asymmetric introduction of rounding errors in floating-point operations is repeated many times, the flow structure finally loses spatial symmetry. Below, we summarize recommended computational approaches effective for symmetry preservation.

- If the initial values are spatially asymmetric, the new physical quantities at symmetric locations are modified to the average of the physical quantities at the symmetric locations.
- The spatial reconstruction should follow the procedures described in section 3.2.2 and 3.2.3. Especially, the THINC reconstruction needs careful implementation because calculations involving non-polynomial functions may yield results that are not exactly correct in floating-point arithmetic, as  $\ln(a) \neq -\ln\left(\frac{1}{a}\right)$ , even if mathematically correct [51].
- The spatial discretization of the wave-propagation method (37) has the addition of three numbers. The term of the total fluctuation should be added later as,

$$\frac{d\bar{q}_i}{dt} = -\frac{1}{\Delta x} \left( \left( \mathcal{A}^+ \Delta Q_{i-\frac{1}{2}} + \mathcal{A}^- \Delta Q_{i+\frac{1}{2}} \right) + \mathcal{A} \Delta Q_i \right). \quad (\text{A.3})$$

- Each fluctuation (43) and (44) has the addition of three numbers due to the wave structures in the HLLC-type solution. We recommend that the waves corresponding to the eigenvalues  $u - c$  and  $u + c$  should be added first as,

$$\mathcal{A}^\pm \Delta Q_{i+\frac{1}{2}} = \left( \left( S_{i+\frac{1}{2}}^1 \right)^\pm \mathcal{W}_{i+\frac{1}{2}}^1 + \left( S_{i+\frac{1}{2}}^3 \right)^\pm \mathcal{W}_{i+\frac{1}{2}}^3 \right) + \left( S_{i+\frac{1}{2}}^2 \right)^\pm \mathcal{W}_{i+\frac{1}{2}}^2, \quad (\text{A.4})$$

$$\mathcal{A} \Delta Q_i = \left( S_i^1 \mathcal{W}_i^1 + S_i^3 \mathcal{W}_i^3 \right) + S_i^2 \mathcal{W}_i^2. \quad (\text{A.5})$$

It is noted that these symmetry-preserving formulations are based on symmetry computational mesh and are required in all space-dimension directions in the multi-dimensional problem.

## Appendix B. Mechanical relaxation

To achieve the mechanical equilibrium between phase 1 and phase 2, pressure relaxation is necessary in the six-equation model. The relaxation equations to be solved read,

$$\frac{\partial \alpha_1}{\partial t} = \mu(p_1 - p_2), \quad (\text{B.1a})$$

$$\frac{\partial(\alpha_1 \rho_1)}{\partial t} = 0, \quad (\text{B.1b})$$

$$\frac{\partial(\alpha_2 \rho_2)}{\partial t} = 0, \quad (\text{B.1c})$$

$$\frac{\partial(\rho \mathbf{u})}{\partial t} = \mathbf{0}, \quad (\text{B.1d})$$

$$\frac{\partial(\alpha_1 E_1)}{\partial t} = -\mu p_1(p_1 - p_2), \quad (\text{B.1e})$$

$$\frac{\partial(\alpha_2 E_2)}{\partial t} = \mu p_1(p_1 - p_2), \quad (\text{B.1f})$$

with assuming the relaxation rate is infinite,  $\mu \rightarrow \infty$ . Variables before and after reaching the mechanical equilibrium state are denoted with superscripts 0 and \*, respectively. The conditions to solve the conservative variables  $q^*$  are derived from (B.1) as,

$$p_1^* = p_2^* \equiv p^*, \quad (\text{B.2a})$$

$$(\alpha_1 \rho_1)^0 = (\alpha_1 \rho_1)^*, \quad (\text{B.2b})$$

$$(\alpha_2 \rho_2)^0 = (\alpha_2 \rho_2)^*, \quad (\text{B.2c})$$

$$(\rho \mathbf{u})^0 = (\rho \mathbf{u})^*, \quad (\text{B.2d})$$

$$\frac{\partial(\alpha_1 E_1)}{\partial t} = -p_1 \frac{\partial \alpha_1}{\partial t}, \quad (\text{B.2e})$$

$$\frac{\partial(\alpha_2 E_2)}{\partial t} = p_1 \frac{\partial \alpha_1}{\partial t}. \quad (\text{B.2f})$$

The relaxed pressure is defined as  $p^*$  in (B.2a). Conditions (B.2b)–(B.2d) mean that  $\alpha_1 \rho_1$ ,  $\alpha_2 \rho_2$ , and  $\rho \mathbf{u}$  are constant in the pressure relaxation, as (B.1b)–(B.1d) indicate. These relations also lead to  $\rho^0 = \rho^*$ ,  $\mathbf{u}^0 = \mathbf{u}^*$  from the mixture rule:  $\alpha_1 \rho_1 + \alpha_2 \rho_2 = \rho$ . Conditions (B.2e) and (B.2f) are obvious from (B.1a), (B.1e), and (B.1f), and lead to  $E^0 = E^*$ . Assuming  $p_1$  is constant, integration of (B.2e) and (B.2f) gives,

$$(\alpha_k E_k)^* - (\alpha_k E_k)^0 = (\alpha_k \mathcal{E}_k)^* - (\alpha_k \mathcal{E}_k)^0 = -p_1(\alpha_k^* - \alpha_k^0), \quad (k = 1, 2), \quad (\text{B.3})$$

using  $\left(\frac{1}{2} \rho \|\mathbf{u}\|^2\right)^0 = \left(\frac{1}{2} \rho \|\mathbf{u}\|^2\right)^*$  and  $\frac{\partial \alpha_1}{\partial t} = -\frac{\partial \alpha_2}{\partial t}$  obtained from  $\alpha_1 + \alpha_2 = 1$ . The phasic total energy  $\mathcal{E}_k$  in (B.3) is calculated using SGEOS (4a), then (B.3) reads,

$$\alpha_k^* = \frac{(\gamma_k - 1)p_1 + p_k^0 + \gamma_k \pi_k}{(\gamma_k - 1)p_1 + p^* + \gamma_k \pi_k} \alpha_k^0, \quad (k = 1, 2), \quad (\text{B.4})$$

with definition (B.2a). Under the assumption  $p_1 = p^*$  [46], we can derive a quadratic equation for  $p^*$  using  $\alpha_1^* + \alpha_2^* = 1$  as,

$$a(p^*)^2 + bp^* + d = 0, \quad (\text{B.5})$$

where

$$a = \gamma_1 \alpha_2^0 + \gamma_2 \alpha_1^0, \quad (\text{B.6a})$$

$$b = -\gamma_1 \alpha_2^0 (p_2^0 - \pi_1) - \gamma_2 \alpha_1^0 (p_1^0 - \pi_2), \quad (\text{B.6b})$$

$$d = -\gamma_1 \alpha_2^0 p_2^0 \pi_1 - \gamma_2 \alpha_1^0 p_1^0 \pi_2. \quad (\text{B.6c})$$

To avoid cancellation of significant digits in floating-point arithmetic, the relaxed pressure  $p^*$  is calculated as follows (see Appendix E),

$$p^* = \begin{cases} \frac{2d}{-b - \sqrt{D}} & \text{if } b > 0, \\ \frac{-b + \sqrt{D}}{2a} & \text{otherwise,} \end{cases} \quad (\text{B.7})$$

where  $D = b^2 - 4ad$ . Once the value of  $p^*$  is obtained,  $\alpha_k^*$  is calculated using (B.4). Other variables that vary in pressure relaxation procedure are updated as,

$$\rho_k^* = \frac{(\alpha_k \rho_k)^0}{\alpha_k^*}, \quad (\text{B.8})$$

$$\mathcal{E}_k^* = \frac{p^* + \gamma_k \pi_k}{\gamma_k - 1} + \eta_k \rho_k^*, \quad (\text{B.9})$$

$$E_k^* = \mathcal{E}_k^* + \frac{1}{2} \rho_k^* \|\mathbf{u}^0\|^2. \quad (\text{B.10})$$

It is noted that these updated variables satisfy *mixture-energy-consistency* (in Definition 3.1 in [18]).

### Appendix C. Thermal relaxation

In this relaxation procedure, the mechanical and thermal equilibrium between phase 1 and phase 2 are achieved. This relaxation is conducted in the interface, as shown in (10). The relaxation equations to be solved read,

$$\frac{\partial \alpha_1}{\partial t} = \mu(p_1 - p_2) + \frac{\theta(T_2 - T_1)}{\kappa}, \quad (\text{C.1a})$$

$$\frac{\partial(\alpha_1 \rho_1)}{\partial t} = 0, \quad (\text{C.1b})$$

$$\frac{\partial(\alpha_2 \rho_2)}{\partial t} = 0, \quad (\text{C.1c})$$

$$\frac{\partial(\rho \mathbf{u})}{\partial t} = \mathbf{0}, \quad (\text{C.1d})$$

$$\frac{\partial(\alpha_1 E_1)}{\partial t} = -\mu p_1 (p_1 - p_2) + \theta(T_2 - T_1), \quad (\text{C.1e})$$

$$\frac{\partial(\alpha_2 E_2)}{\partial t} = \mu p_1 (p_1 - p_2) - \theta(T_2 - T_1), \quad (\text{C.1f})$$

with assuming the relaxation rates are infinite,  $\mu, \theta \rightarrow \infty$ . Variables before and after reaching the thermal equilibrium state are denoted with superscripts 0 and \*\*, respectively. The conditions to solve the conservative variables  $q^{**}$  are derived from (C.1) as,

$$p_1^{**} = p_2^{**} \equiv p^{**}, \quad (\text{C.2a})$$

$$T_1^{**} = T_2^{**} \equiv T^{**}, \quad (\text{C.2b})$$

$$(\alpha_1 \rho_1)^0 = (\alpha_1 \rho_1)^{**}, \quad (\text{C.2c})$$

$$(\alpha_2 \rho_2)^0 = (\alpha_2 \rho_2)^{**}, \quad (\text{C.2d})$$

$$(\rho \mathbf{u})^0 = (\rho \mathbf{u})^{**}, \quad (\text{C.2e})$$

$$E^0 = E^{**}. \quad (\text{C.2f})$$

The relaxed pressure and temperature are defined as  $p^{**}$  in (C.2a) and as  $T^{**}$  in (C.2b) respectively. From (C.2c) and (C.2d), in the thermal relaxation the mixture density  $\rho = \alpha_1 \rho_1 + \alpha_2 \rho_2$  is constant, and then the mass fraction  $Y_k = \frac{\alpha_k \rho_k}{\rho}$  is also constant. From (C.2e) and (C.2f), the mixture internal energy  $\mathcal{E}$  is constant. Then, the mixture rules (2a) and (2c) after the thermal relaxation read,

$$\frac{Y_1^0}{\rho_1^{**}(p^{**}, T^{**})} + \frac{Y_2^0}{\rho_2^{**}(p^{**}, T^{**})} = \frac{1}{\rho^0}, \quad (\text{C.3a})$$

$$\frac{Y_1^0 \mathcal{E}_1^{**}(p^{**}, T^{**})}{\rho_1^{**}(p^{**}, T^{**})} + \frac{Y_2^0 \mathcal{E}_2^{**}(p^{**}, T^{**})}{\rho_2^{**}(p^{**}, T^{**})} = \frac{\mathcal{E}^0}{\rho^0}. \quad (\text{C.3b})$$

We note that both the phase density  $\rho_k$  and phase internal energy  $\mathcal{E}_k$  can be a function of the pressure  $p_k$  and temperature  $T_k$  from SGEOS formulations (4a) and (4b). From (C.3), we can derive a quadratic equation for  $p^{**}$  as,

$$a'(p^{**})^2 + b'p^{**} + d' = 0, \quad (\text{C.4})$$

where

$$a' = Y_1^0 C_{v1} + Y_2^0 C_{v2}, \quad (\text{C.5a})$$

$$b' = Y_1^0 C_{v1} (\gamma_1 \pi_1 + \pi_2 - (\gamma_1 - 1) \hat{\mathcal{E}}^0) + Y_2^0 C_{v2} (\gamma_2 \pi_2 + \pi_1 - (\gamma_2 - 1) \hat{\mathcal{E}}^0), \quad (\text{C.5b})$$

$$d' = Y_1^0 C_{v1} \pi_2 (\gamma_1 \pi_1 - (\gamma_1 - 1) \hat{\mathcal{E}}^0) + Y_2^0 C_{v2} \pi_1 (\gamma_2 \pi_2 - (\gamma_2 - 1) \hat{\mathcal{E}}^0). \quad (\text{C.5c})$$

Here,  $\hat{\mathcal{E}}^0 \equiv \mathcal{E}^0 - ((\alpha_1 \rho_1)^0 \eta_1 + (\alpha_2 \rho_2)^0 \eta_2)$ . The relaxed pressure  $p^{**}$  is calculated as follows (see Appendix E),

$$p^{**} = \begin{cases} \frac{2d'}{-b' - \sqrt{D'}} & \text{if } b' > 0, \\ \frac{-b' + \sqrt{D'}}{2a'} & \text{otherwise,} \end{cases} \quad (\text{C.6})$$

where  $D' = b'^2 - 4a'd'$ . Once the value of  $p^{**}$  is obtained, other variables that vary in thermal relaxation procedure are updated as,

$$\alpha_1^{**} = \frac{C_{v1}(\gamma_1 - 1)(p^{**} + \pi_2)(\alpha_1 \rho_1)^0}{C_{v1}(\gamma_1 - 1)(p^{**} + \pi_2)(\alpha_1 \rho_1)^0 + C_{v2}(\gamma_2 - 1)(p^{**} + \pi_1)(\alpha_2 \rho_2)^0}, \quad (\text{C.7})$$

$$\rho_k^{**} = \frac{(\alpha_k \rho_k)^0}{\alpha_k^{**}}, \quad (\text{C.8})$$

$$\mathcal{E}_k^{**} = \frac{p^{**} + \gamma_k \pi_k}{\gamma_k - 1} + \eta_k \rho_k^{**}, \quad (\text{C.9})$$

$$E_k^{**} = \mathcal{E}_k^{**} + \frac{1}{2} \rho_k^{**} \|\mathbf{u}^0\|^2. \quad (\text{C.10})$$

## Appendix D. Chemical relaxation

In this relaxation procedure, the mechanical, thermal, and chemical equilibrium between phase 1 and phase 2 are achieved. This relaxation is conducted in the interface under the metastable condition, as shown in (11). The relaxation equations to be solved read,

$$\frac{\partial \alpha_1}{\partial t} = \mu(p_1 - p_2) + \frac{\theta(T_2 - T_1)}{\kappa} + \frac{\nu(g_2 - g_1)}{\rho_1}, \quad (\text{D.1a})$$

$$\frac{\partial(\alpha_1 \rho_1)}{\partial t} = \nu(g_2 - g_1), \quad (\text{D.1b})$$

$$\frac{\partial(\alpha_2 \rho_2)}{\partial t} = -\nu(g_2 - g_1), \quad (\text{D.1c})$$

$$\frac{\partial(\rho \mathbf{u})}{\partial t} = \mathbf{0}, \quad (\text{D.1d})$$

$$\frac{\partial(\alpha_1 E_1)}{\partial t} = -\mu p_1(p_1 - p_2) + \theta(T_2 - T_1) + \nu e_1(g_2 - g_1), \quad (\text{D.1e})$$

$$\frac{\partial(\alpha_2 E_2)}{\partial t} = \mu p_1(p_1 - p_2) - \theta(T_2 - T_1) - \nu e_1(g_2 - g_1), \quad (\text{D.1f})$$

with assuming the relaxation rates are infinite,  $\mu, \theta, \nu \rightarrow \infty$ . Variables before and after reaching the chemical equilibrium state are denoted with superscripts 0 and  $\otimes$ , respectively. The conditions to solve the conservative variables  $\mathbf{q}^\otimes$  are derived from (D.1) as,

$$p_1^\otimes = p_2^\otimes \equiv p^\otimes, \quad (\text{D.2a})$$

$$T_1^\otimes = T_2^\otimes \equiv T^\otimes, \quad (\text{D.2b})$$

$$g_1^\circledast = g_2^\circledast, \quad (\text{D.2c})$$

$$\rho^0 = \rho^\circledast, \quad (\text{D.2d})$$

$$(\rho \mathbf{u})^0 = (\rho \mathbf{u})^\circledast, \quad (\text{D.2e})$$

$$E^0 = E^\circledast. \quad (\text{D.2f})$$

The relaxed pressure and temperature are defined as  $p^\circledast$  in (D.2a) and as  $T^\circledast$  in (D.2b) respectively. From (D.2d)–(D.2f), the mixture internal energy  $\mathcal{E}$  is constant in the chemical relaxation. Similar to the case of the thermal relaxation procedure, using the mixture rules (2a) and (2c) after the chemical relaxation we obtain,

$$\frac{Y_1^\circledast}{\rho_1^\circledast(p^\circledast, T^\circledast)} + \frac{Y_2^\circledast}{\rho_2^\circledast(p^\circledast, T^\circledast)} = \frac{1}{\rho^0}, \quad (\text{D.3a})$$

$$\frac{Y_1^\circledast \mathcal{E}_1^\circledast(p^\circledast, T^\circledast)}{\rho_1^\circledast(p^\circledast, T^\circledast)} + \frac{Y_2^\circledast \mathcal{E}_2^\circledast(p^\circledast, T^\circledast)}{\rho_2^\circledast(p^\circledast, T^\circledast)} = \frac{\mathcal{E}^0}{\rho^0}. \quad (\text{D.3b})$$

In this case, the mass fraction  $Y_k$  is not constant.  $Y_1^\circledast$  and  $Y_2^\circledast$  in (D.3) can be eliminated using  $Y_1^\circledast + Y_2^\circledast = 1$ . Then, a quadratic equation for  $T^\circledast(p^\circledast)$  can be derived as,

$$a_p(p^\circledast)(T^\circledast(p^\circledast))^2 + b_p(p^\circledast)T^\circledast(p^\circledast) + d_p(p^\circledast) = 0, \quad (\text{D.4})$$

where

$$a_p(p^\circledast) = \rho^0 C_{v1} C_{v2} ((\gamma_2 - 1)(p^\circledast + \gamma_1 \pi_1) - (\gamma_1 - 1)(p^\circledast + \gamma_2 \pi_2)), \quad (\text{D.5a})$$

$$b_p(p^\circledast) = C_{v2}(p^\circledast + \pi_1)(p^\circledast + \gamma_2 \pi_2 - (\gamma_2 - 1)(\mathcal{E}^0 - \rho^0 \eta_1)) \\ - C_{v1}(p^\circledast + \pi_2)(p^\circledast + \gamma_1 \pi_1 - (\gamma_1 - 1)(\mathcal{E}^0 - \rho^0 \eta_2)), \quad (\text{D.5b})$$

$$d_p(p^\circledast) = (\eta_2 - \eta_1)(p^\circledast + \pi_1)(p^\circledast + \pi_2). \quad (\text{D.5c})$$

The temperature  $T^\circledast(p^\circledast)$  is calculated as follows (see Appendix E),

$$T^\circledast(p^\circledast) = \begin{cases} \frac{2d_p(p^\circledast)}{-b_p(p^\circledast) - \sqrt{D_p(p^\circledast)}} & \text{if } b_p(p^\circledast) > 0, \\ \frac{-b_p(p^\circledast) + \sqrt{D_p(p^\circledast)}}{2a_p(p^\circledast)} & \text{otherwise,} \end{cases} \quad (\text{D.6})$$

where  $D_p(p^\circledast) = b_p(p^\circledast)^2 - 4a_p(p^\circledast)d_p(p^\circledast)$ . Then, substituting  $T^\circledast(p^\circledast)$  into p-T saturation curve (D.2c):

$$A_s + \frac{B_s}{T^\circledast(p^\circledast)} + C_s \ln T^\circledast(p^\circledast) + D_s \ln(p^\circledast + \pi_1) - \ln(p^\circledast + \pi_2) = 0, \quad (\text{D.7})$$

the relaxed pressure  $p^\circledast$  can be obtained. As unfortunately  $p^\circledast$  cannot be solved explicitly, the Newton-Raphson method can be used to numerically solve  $p^\circledast$ . Once the value of  $p^\circledast$  is obtained,  $T$  is calculated using (D.6). Other variables that vary in the thermal relaxation procedure are updated as,

$$\rho_k^\circledast = \frac{p^\circledast + \pi_k}{(\gamma_k - 1)C_{vk}T^\circledast}, \quad (\text{D.8})$$

$$a_1^\circledast = \frac{\rho^0 - \rho_2^\circledast}{\rho_1^\circledast - \rho_2^\circledast}, \quad (\text{D.9})$$

$$\mathcal{E}_k^\circledast = \frac{p^\circledast + \gamma_k \pi_k}{\gamma_k - 1} + \eta_k \rho_k^\circledast, \quad (\text{D.10})$$

$$E_k^\circledast = \mathcal{E}_k^\circledast + \frac{1}{2} \rho_k^\circledast \|\mathbf{u}^0\|^2. \quad (\text{D.11})$$

It is noted that instead of this chemical relaxation procedure, an approximate solver [61] is also available to obtain the relaxed pressure and temperature.

## Appendix E. Cancellation of significant digits in solving quadratic equation

The real solution of the quadratic equation:  $ax^2 + bx + c = 0$  is usually expressed as,

$$x_1 = \frac{-b - \sqrt{D}}{2a}, \quad x_2 = \frac{-b + \sqrt{D}}{2a}, \quad (D \equiv b^2 - 4ac \geq 0). \quad (\text{E.1})$$

However, in a numerical sense, the solutions (E.1) can generate considerable errors due to the “cancellation of significant digits” in floating-point arithmetic. This happens in the case that  $-b \pm \sqrt{D} \approx 0$ . One of the well-known remedies for this issue is as follows,

$$x_1 = \begin{cases} \frac{-b-\sqrt{D}}{2a} & \text{if } b > 0, \\ \frac{2c}{-b+\sqrt{D}} & \text{otherwise,} \end{cases} \quad x_2 = \begin{cases} \frac{2c}{-b-\sqrt{D}} & \text{if } b > 0, \\ \frac{-b+\sqrt{D}}{2a} & \text{otherwise.} \end{cases} \quad (\text{E.2})$$

Note that although (E.2) is implemented, the cancellation of significant digits cannot be avoided in the case that the solutions are almost the multiple roots ( $D \approx 0$ ).

## References

- [1] C.W. Hirt, B.D. Nichols, Volume of fluid (VOF) method for the dynamics of free boundaries, *J. Comput. Phys.* 39 (1981) 201–225.
- [2] D.B. Kothe, W.J. Rider, Reconstructing volume tracking, *J. Comput. Phys.* 141 (1998) 112–152.
- [3] S.W. Welch, J. Wilson, A volume of fluid based method for fluid flows with phase change, *J. Comput. Phys.* 160 (2000) 662–682, <https://doi.org/10.1006/jcph.2000.6481>.
- [4] W. Mulder, S. Osher, J.A. Sethian, Computing interface motion in compressible gas dynamics, *J. Comput. Phys.* 100 (1992) 209–228, [https://doi.org/10.1016/0021-9991\(92\)90229-R](https://doi.org/10.1016/0021-9991(92)90229-R).
- [5] M. Sussman, A level set approach for computing solutions to incompressible two-phase flow, *J. Comput. Phys.* 114 (1) (1994) 146–159, <https://doi.org/10.1006/jcph.1994.1155>.
- [6] S.O. Unverdi, G. Tryggvason, A front-tracking method for viscous, incompressible, multi-fluid flows, *J. Comput. Phys.* 100 (1992) 25–37, [https://doi.org/10.1016/0021-9991\(92\)90307-K](https://doi.org/10.1016/0021-9991(92)90307-K).
- [7] G. Tryggvason, B. Bunner, A. Esmaeili, D. Juric, N. Al-Rawahi, W. Tauber, J. Han, S. Nas, Y.J. Jan, A front-tracking method for the computations of multiphase flow, *J. Comput. Phys.* 169 (2001) 708–759, <https://doi.org/10.1006/jcph.2001.6726>.
- [8] Richard Saurel, F. Petitpas, R.A. Berry, Simple and efficient relaxation methods for interfaces separating compressible fluids, cavitating flows and shocks in multiphase mixtures, *J. Comput. Phys.* 228 (2009) 1678–1712, <https://doi.org/10.1016/j.jcp.2008.11.002>.
- [9] M.R. Baer, J.W. Nunziato, A two-phase mixture theory for the deflagration-to-detonation transition (ddt) in reactive granular materials, *Int. J. Multiph. Flow* 12 (1986) 861–889, [https://doi.org/10.1016/0301-9322\(86\)90033-9](https://doi.org/10.1016/0301-9322(86)90033-9).
- [10] R. Saurel, R. Abgrall, A multiphase Godunov method for compressible multifluid and multiphase flows, *J. Comput. Phys.* 150 (1999) 425–467, <https://doi.org/10.1006/jcph.1999.6187>.
- [11] A. Zein, M. Hantke, G. Warnecke, Modeling phase transition for compressible two-phase flows applied to metastable liquids, *J. Comput. Phys.* 229 (2010) 2964–2998, <https://doi.org/10.1016/j.jcp.2009.12.026>.
- [12] R. Abgrall, How to prevent pressure oscillations in multicomponent flow calculations: a quasi conservative approach, *J. Comput. Phys.* 125 (1996) 150–160, <https://doi.org/10.1006/jcph.1996.0085>.
- [13] K.M. Shyue, A fluid-mixture type algorithm for compressible multicomponent flow with Mie-Grüneisen equation of state, *J. Comput. Phys.* 171 (2001) 678–707, <https://doi.org/10.1006/jcph.2001.6801>.
- [14] A.K. Kapila, R. Menikoff, J.B. Dzilil, S.F. Son, D.S. Stewart, Two-phase modeling of deflagration-to-detonation transition in granular materials: reduced equations, *Phys. Fluids* 13 (2001) 3002–3024, <https://doi.org/10.1063/1.1398042>.
- [15] G. Allaire, S. Clerc, S. Kokh, A five-equation model for the simulation of interfaces between compressible fluids, *J. Comput. Phys.* 181 (2002) 577–616, <https://doi.org/10.1006/jcph.2002.7143>.
- [16] F. Petitpas, E. Franquet, R. Saurel, O. Le Metayer, A relaxation-projection method for compressible flows. Part II: Artificial heat exchanges for multiphase shocks, *J. Comput. Phys.* 225 (2007) 2214–2248, <https://doi.org/10.1016/j.jcp.2007.03.014>.
- [17] F. Petitpas, R. Saurel, E. Franquet, A. Chinnayya, Modelling detonation waves in condensed energetic materials: multiphase CJ conditions and multidimensional computations, *Shock Waves* 19 (2009) 377–401, <https://doi.org/10.1007/s00193-009-0217-7>.
- [18] M. Pelanti, K.M. Shyue, A mixture-energy-consistent six-equation two-phase numerical model for fluids with interfaces, cavitation and evaporation waves, *J. Comput. Phys.* 259 (2014) 331–357, <https://doi.org/10.1016/j.jcp.2013.12.003>.
- [19] S.K. Godunov, A difference method for numerical calculation of discontinuous solutions of the equations of hydrodynamics, *Math. Sb.* 47 (1959) 271–306.
- [20] B. Van Leer, Towards the ultimate conservative difference scheme. IV. A new approach to numerical convection, *J. Comput. Phys.* 23 (1977) 276–299, [https://doi.org/10.1016/0021-9991\(77\)90095-X](https://doi.org/10.1016/0021-9991(77)90095-X).
- [21] X.-D. Liu, S. Osher, T. Chan, Weighted essentially non-oscillatory schemes, *J. Comput. Phys.* 115 (1994) 200–212, <https://doi.org/10.1002/flid.3889>.
- [22] G.-S. Jiang, C.-W. Shu, Efficient implementation of weighted ENO schemes, *J. Comput. Phys.* 126 (1996) 202–228.
- [23] R. Borges, M. Carmona, B. Costa, W.S. Don, An improved weighted essentially non-oscillatory scheme for hyperbolic conservation laws, *J. Comput. Phys.* 227 (2008) 3191–3211, <https://doi.org/10.1016/j.jcp.2007.11.038>.
- [24] A. Suresh, H. Huynh, Accurate monotonicity-preserving schemes with Runge–Kutta time stepping, *J. Comput. Phys.* 136 (1997) 83–99, <https://doi.org/10.1006/jcph.1997.5745>.
- [25] Z. He, Y. Zhang, F. Gao, X. Li, B. Tian, An improved accurate monotonicity-preserving scheme for the Euler equations, *Comput. Fluids* 140 (2016) 1–10, <https://doi.org/10.1016/j.compfluid.2016.09.002>.
- [26] A. Harten, High resolution schemes for hyperbolic conservation laws, *Int. J. Numer. Methods Fluids* 23 (1983) 309–323, [https://doi.org/10.1002/\(SICI\)1097-0363\(19960830\)23:4<309::AID-FLD410>3.0.CO;2-Z](https://doi.org/10.1002/(SICI)1097-0363(19960830)23:4<309::AID-FLD410>3.0.CO;2-Z).
- [27] Z. Sun, S. Inaba, F. Xiao, Boundary variation diminishing (BVD) reconstruction: a new approach to improve Godunov schemes, *J. Comput. Phys.* 322 (2016) 309–325, <https://doi.org/10.1016/j.jcp.2016.06.051>.
- [28] X. Deng, S. Inaba, B. Xie, K.M. Shyue, F. Xiao, High fidelity discontinuity-resolving reconstruction for compressible multiphase flows with moving interfaces, *J. Comput. Phys.* 371 (2018) 945–966, <https://doi.org/10.1016/j.jcp.2018.03.036>.
- [29] X. Deng, B. Xie, R. Loubère, Y. Shimizu, F. Xiao, Limiter-free discontinuity-capturing scheme for compressible gas dynamics with reactive fronts, *Comput. Fluids* 171 (2018) 1–14, <https://doi.org/10.1016/j.compfluid.2018.05.015>.
- [30] X. Deng, Y. Shimizu, F. Xiao, A fifth-order shock capturing scheme with two-stage boundary variation diminishing algorithm, *J. Comput. Phys.* 386 (2019) 323–349, <https://doi.org/10.1016/j.jcp.2019.02.024>.
- [31] X. Deng, Y. Shimizu, B. Xie, F. Xiao, Constructing higher order discontinuity-capturing schemes with upwind-biased interpolations and boundary variation diminishing algorithm, *Comput. Fluids* 200 (2020) 104433, <https://doi.org/10.1016/j.compfluid.2020.104433>.
- [32] S. Tann, X. Deng, Y. Shimizu, R. Loubère, F. Xiao, Solution property preserving reconstruction for finite volume scheme: a boundary variation diminishing+multidimensional optimal order detection framework, *Int. J. Numer. Methods Fluids* 92 (2020) 603–634, <https://doi.org/10.1002/flid.4798>.

- [33] S. Tann, X. Deng, R. Loubère, F. Xiao, Solution property preserving reconstruction BVD+MOOD scheme for compressible Euler equations with source terms and detonations, *Comput. Fluids* 206 (2020) 104594, <https://doi.org/10.1016/j.compfluid.2020.104594>.
- [34] L. Cheng, X. Deng, B. Xie, Y. Jiang, F. Xiao, Low-dissipation BVD schemes for single and multi-phase compressible flows on unstructured grids, *J. Comput. Phys.* 428 (2021) 110088, <https://doi.org/10.1016/j.jcp.2020.110088>.
- [35] Q. Li, K. Yokoi, Z. Xie, S. Omar, J. Xue, A fifth-order high-resolution shock-capturing scheme based on modified weighted essentially non-oscillatory method and boundary variation diminishing framework for compressible flows and compressible two-phase flows, *Phys. Fluids* 33 (2021), <https://doi.org/10.1063/5.0045635>.
- [36] A.S. Chamarithi, S.H. Frankel, High-order central-upwind shock capturing scheme using a boundary variation diminishing (BVD) algorithm, *J. Comput. Phys.* 427 (2021) 110067, <https://doi.org/10.1016/j.jcp.2020.110067>.
- [37] Y. Majima, H. Wakimura, T. Aoki, F. Xiao, A new high-fidelity total variation diminishing scheme based on the boundary variation diminishing principle for compressible flows, *Comput. Fluids* 266 (2023) 106070, <https://doi.org/10.1016/j.compfluid.2023.106070>.
- [38] F. Xiao, Y. Honma, T. Kono, A simple algebraic interface capturing scheme using hyperbolic tangent function, *Int. J. Numer. Methods Fluids* 48 (2005) 1023–1040, <https://doi.org/10.1002/fld.975>.
- [39] F. Xiao, S. Li, C. Chen, Revisit to the THINC scheme: a simple algebraic VOF algorithm, *J. Comput. Phys.* 230 (2011) 7086–7092, <https://doi.org/10.1016/j.jcp.2011.06.012>.
- [40] F. Zhang, J. Cheng, A bound-preserving and positivity-preserving finite volume WENO scheme for solving five-equation model of two-medium flows, *Commun. Nonlinear Sci. Numer. Simul.* 114 (2022) 106649, <https://doi.org/10.1016/j.cnsns.2022.106649>.
- [41] D.J. Picard, P.R. Bishnoi, Calculation of the thermodynamic sound velocity in two-phase multicomponent fluids, *Int. J. Multiph. Flow* 13 (1987) 295–308, [https://doi.org/10.1016/0301-9322\(87\)90050-4](https://doi.org/10.1016/0301-9322(87)90050-4).
- [42] T. Flåtten, H. Lund, Relaxation two-phase flow models and the subcharacteristic condition, *Math. Models Methods Appl. Sci.* 21 (2011) 2379–2407, <https://doi.org/10.1142/S0218202511005775>.
- [43] R. Saurel, F. Petitpas, R. Abgrall, Modelling phase transition in metastable liquids: application to cavitating and flashing flows, *J. Fluid Mech.* 607 (2008) 313–350, <https://doi.org/10.1017/S0022112008002061>.
- [44] F. Petitpas, J. Massoni, R. Saurel, E. Lapebie, L. Munier, Diffuse interface model for high speed cavitating underwater systems, *Int. J. Multiph. Flow* 35 (2009) 747–759, <https://doi.org/10.1016/j.ijmultiphaseflow.2009.03.011>.
- [45] G. Faccanoni, S. Kokh, G. Allaire, Modelling and simulation of liquid-vapor phase transition in compressible flows based on thermodynamical equilibrium, *Modél. Math. Anal. Numér.* 46 (2012) 1029–1054, <https://doi.org/10.1051/m2an/2011069>.
- [46] M. Pelanti, K.M. Shyue, A numerical model for multiphase liquid–vapor–gas flows with interfaces and cavitation, *Int. J. Multiph. Flow* 113 (2019) 208–230, <https://doi.org/10.1016/j.ijmultiphaseflow.2019.01.010>.
- [47] O. Le Métayer, J. Massoni, R. Saurel, Modelling evaporation fronts with reactive Riemann solvers, *J. Comput. Phys.* 205 (2005) 567–610, <https://doi.org/10.1016/j.jcp.2004.11.021>.
- [48] M. De Lorenzo, M. Pelanti, P. Lafon, HLLC-type and path-conservative schemes for a single-velocity six-equation two-phase flow model: a comparative study, *Appl. Math. Comput.* 333 (2018) 95–117, <https://doi.org/10.1016/j.amc.2018.03.092>.
- [49] S. Gottlieb, C.-w. Shu, E. Tadmor, Strong stability-preserving high-order time discretization, *SIAM Rev.* 43 (2001) 89–112.
- [50] B. van Leer, Towards the ultimate conservative difference scheme. II. Monotonicity and conservation combined in a second-order scheme, *J. Comput. Phys.* 14 (1974) 361–370, [https://doi.org/10.1016/0021-9991\(74\)90019-9](https://doi.org/10.1016/0021-9991(74)90019-9).
- [51] H. Wakimura, S. Takagi, F. Xiao, Symmetry-preserving enforcement of low-dissipation method based on boundary variation diminishing principle, *Comput. Fluids* 233 (2022) 105227, <https://doi.org/10.1016/j.compfluid.2021.105227>, <http://arxiv.org/abs/2106.01872>.
- [52] X. Deng, Z.h. Jiang, P. Vincent, F. Xiao, C. Yan, A new paradigm of dissipation-adjustable, multi-scale resolving schemes for compressible flows, *J. Comput. Phys.* 466 (2022) 111287, <https://doi.org/10.1016/j.jcp.2022.111287>.
- [53] S. Takagi, L. Fu, H. Wakimura, F. Xiao, A novel high-order low-dissipation TENO-THINC scheme for hyperbolic conservation laws, *J. Comput. Phys.* 452 (2021) 110899, <https://doi.org/10.1016/j.jcp.2021.110899>.
- [54] S. Takagi, H. Wakimura, L. Fu, F. Xiao, High-order low-dissipation shock-resolving TENO-THINC schemes for hyperbolic conservation laws, *Commun. Comput. Phys.* 34 (2023) 1043–1078, <https://doi.org/10.4208/cicp.OA-2023-0061>.
- [55] Z. He, Y. Ruan, Y. Yu, B. Tian, F. Xiao, Self-adjusting steepness-based schemes that preserve discontinuous structures in compressible flows, *J. Comput. Phys.* 463 (2022) 111268, <https://doi.org/10.1016/j.jcp.2022.111268>.
- [56] R.J. LeVeque, Wave propagation algorithms for multidimensional hyperbolic systems, *J. Comput. Phys.* 131 (1997) 327–353, <https://doi.org/10.1006/jcph.1996.5603>.
- [57] D.I. Ketcheson, M. Parsani, R.J. LeVeque, High-order wave propagation algorithms for hyperbolic systems, *SIAM J. Sci. Comput.* 35 (2013) A351–A377, <https://doi.org/10.1137/110830320>.
- [58] K.M. Shyue, An efficient shock-capturing algorithm for compressible multicomponent problems, *J. Comput. Phys.* 142 (1998) 208–242, <https://doi.org/10.1006/jcph.1998.5930>.
- [59] K.M. Shyue, F. Xiao, An Eulerian interface sharpening algorithm for compressible two-phase flow: the algebraic THINC approach, *J. Comput. Phys.* 268 (2014) 326–354, <https://doi.org/10.1016/j.jcp.2014.03.010>.
- [60] E.F. Toro, *Riemann Solvers and Numerical Methods for Fluid Dynamics*, Springer, 2009.
- [61] A. Chiapolino, P. Boivin, R. Saurel, A simple phase transition relaxation solver for liquid–vapor flows, *Int. J. Numer. Methods Fluids* 83 (2017) 583–605, <https://doi.org/10.1002/fld.4282>.
- [62] F. Caro, F. Coquel, D. Jamet, S. Kokh, A simple finite-volume method for compressible isothermal two-phase flows simulation, *Int. J. Finite Vol.* 6 (2006), <https://hal.science/hal-01114190>.
- [63] J. Zhang, A simple and effective five-equation two-phase numerical model for liquid-vapor phase transition in cavitating flows, *Int. J. Multiph. Flow* 132 (2020) 103417, <https://doi.org/10.1016/j.ijmultiphaseflow.2020.103417>.
- [64] R.J. LeVeque, *Finite Volume Methods for Hyperbolic Problems*, Cambridge University Press, 2004.
- [65] N. Fleischmann, S. Adami, N.A. Adams, Numerical symmetry-preserving techniques for low-dissipation shock-capturing schemes, *Comput. Fluids* 189 (2019) 94–107, <https://doi.org/10.1016/j.compfluid.2019.04.004>.